Simulating the one-dimensional structure of Titan's upper atmosphere: 1. Formulation of the Titan Global Ionosphere-Thermosphere Model and benchmark simulations

Jared M. Bell,[1] Stephen W. Bougher,[2] J. Hunter Waite Jr.,[1] Aaron J. Ridley,[2] Brian A. Magee,[1] Kathleen E. Mandt,[1] Joseph Westlake,[3] Anna D. DeJong,[1] Akiva Bar–Nun,[4] Ronen Jacovi,[5] Gabor Toth,[2] and Virginie De La Haye[1]

[1] We employ a newly developed Navier-Stokes model, the Titan Global Ionosphere-Thermosphere Model (T-GITM) to address the one dimensional (1-D) coupled composition, dynamics, and energetics of Titan's upper atmosphere. Our main goals are to delineate the details of this new theoretical tool and to present benchmark calibration simulations compared against the Ion-Neutral Mass Spectrometer (INMS) neutral density measurements. First, we outline the key physical routines contained in T-GITM and their computational formulation. Then, we compare a series of model simulations against recent 1-D work by Cui et al. (2008), Strobel (2008, 2009), and Yelle et al. (2008) in order to provide a fiducial for calibrating this new model. In paper 2 and a future paper, we explore the uncertainties in our knowledge of Titan's atmosphere between ~500 km and 1000 km in order to determine how the present measurements constrain our theoretical understanding of atmospheric structures and processes.

Citation: Bell, J. M., et al. (2010), Simulating the one-dimensional structure of Titan's upper atmosphere: 1. Formulation of the Titan Global Ionosphere-Thermosphere Model and benchmark simulations, *J. Geophys. Res.*, *115*, E12002, doi:10.1029/2010JE003636.

1. Introduction and Scientific Motivation

[2] Titan, the second largest satellite in the solar system, possesses an equatorial radius of 2575 km and enough gravity to maintain a permanent nitrogen and methane rich atmosphere of 1.5 bars at its surface. Thick organic hazes encircle this Kronian moon, masking its solid surface from view. This combination of ubiquitous organic compounds and a nitrogen atmosphere has led some researchers to speculate that Titan may represent a cryogenic version of a pre-biotic Earth [*Sagan and Thompson*, 1984; *Clarke and Ferris*, 1997].

[3] With the arrival of the Cassini-Huygens mission to Titan, scientists now have a chance to study this fascinating satellite to an unprecedented degree, using a plethora of both in situ and remote observations [*Achterberg et al.*, 2008; *Flasar et al.*, 2005; *Niemann et al.*, 2005; *Shemansky et al.*, 2005; *Teanby et al.*, 2007; *Waite et al.*, 2005, 2006]. However, interpreting measurements without a self-consistent theoretical context can represent a daunting and potentially misleading task. Thus, in this work, we unveil a new theoretical tool, the Titan Global Ionosphere-Thermosphere Model (T-GITM), which allows for self-consistent investigations into the composition, energetics, and dynamics of Titan's upper atmosphere.

1.1. Ion-Neutral Mass Spectrometer Data

[4] Currently two independent methods have emerged to analyze the Cassini Ion-Neutral Mass Spectrometer (INMS) raw data. The first published method was that of *Cui et al.* [2009]. This method has been used in the works of *Cui et al.* [2008], *Krasnopolsky* [2009], *Müller-Wodarg et al.* [2008], *Strobel* [2009], and *Yelle et al.* [2008]. Another method has been developed and utilized since the start of the Cassini mission and is described by *Magee et al.* [2009]. This latter data reduction method was employed in works by *Crary et al.* [2009], *Cravens et al.* [2009], *De La Haye et al.* [2007a, 2007b, 2008b], *Mandt et al.* [2009], *Robertson et al.* [2009], and *Waite et al.* [2005, 2007, 2009].

[5] For the purposes of the current study, we utilize the neutral density measurements from *Magee et al.* [2009] as a basis for comparison. However, in order to calibrate against the works of *Cui et al.* [2008], *Strobel* [2008, 2009], and *Yelle et al.* [2008], we compare simulated ^{40}Ar mixing ratios with those derived from the analysis by *Yelle et al.* [2008].

[1]Division of Space Science and Engineering, Southwest Research Institute, San Antonio, Texas, USA.

[2]Department of Atmospheric, Oceanic, and Space Sciences, University of Michigan, Ann Arbor, Michigan, USA.

[3]Department of Physics and Astronomy, University of Texas at San Antonio, San Antonio, Texas, USA.

[4]Department of Geophysics and Planetary Sciences, Tel Aviv University, Tel Aviv, Israel.

[5]Ice Spectroscopy Laboratory, Jet Propulsion Laboratory, California Institute of Technology, Pasadena, California, USA.

Although there are significant and scientifically important differences between the composition determinations of *Cui et al.* [2009] and *Magee et al.* [2009], we must defer this topic to paper 2. In Summary, all of the data shown here is taken from *Magee et al.* [2009], except for the ^{40}Ar Mixing ratios in Figure 3.

1.2. Purpose of This Study

[6] The primary focus of this investigation is to provide a series of benchmark calibration simulations for the Titan Global Ionosphere-Thermosphere Model. In order to accomplish this goal, section 2 delineates the specifics of T-GITM, enumerating the many physical components comprising this framework in one dimension. Section 3 presents a series of simulations that are meant to be directly compared with other recent one dimensional (1-D) modeling results of Titan's upper atmosphere. Section 4 discusses the coupling between the simulated dynamics, composition, and energetics in Titan's upper atmosphere and outlines how these benchmark simulations compare with the works of *Cui et al.* [2008], *Strobel* [2008, 2009], and *Yelle et al.* [2008].

2. Titan Global Ionosphere-Thermosphere Modeling Framework

[7] T-GITM is based upon an existing Earth Global Ionosphere-Thermosphere Model (GITM), developed at the University of Michigan and detailed by *Ridley et al.* [2006]. This numerical framework possesses three key characteristics that distinguish it from preexisting hydrostatic general circulation models (GCMs). First, the GITM framework utilizes spherical polar coordinates to solve the Navier-Stokes system of equations [*Schunk and Nagy*, 2000; *Gombosi*, 1999]. Thus, the radial distance from the planetary center, r, serves as the vertical coordinate, instead of using pressure levels as in previous GCMs [e.g., *Roble et al.*, 1988; *Fuller-Rowell and Rees*, 1980].

[8] This formulation allows the planetary gravitational acceleration to vary explicitly with altitude, which is important for an extended atmosphere such as Titan's. *Müller-Wodarg et al.* [2000] explored the ramifications of employing a formulation of gravity given at the mean altitude of a pressure level versus employing a constant gravity across the entire calculation domain (600–1400 km) at Titan. The authors found that this introduced negligible differences in their calculated dynamical fields, but indicated that a gravitational force that varied with altitude could have important implications for Titan's upper atmosphere.

[9] Second, GITM does not enforce hydrostatic equilibrium at all points in the atmosphere. Differences between pressure gradient and gravitational forces can become significant, appreciably modifying the thermosphere's dynamics [*Deng et al.*, 2008]. Third, GITM explicitly calculates vertical transport from the radial momentum equation. Other hydrostatic General Circulation Models (GCMs) first calculate the horizontal velocities, u_θ, u_ϕ, and then derive the vertical velocities by demanding that $\nabla \cdot \mathbf{u} = 0$ throughout the calculation domain [*Roble et al.*, 1988; *Roble and Ridley*; 1994; *Fuller-Rowell and Rees*, 1980, 1983].

[10] In recent work by *Deng et al.* [2008] and *Boqueho and Blelly* [2005], vertical velocities prove to impact the thermosphere's composition and energetics significantly. In particular, *Boqueho and Blelly* [2005] demonstrate that, at Mars, the divergence of the vertical winds modifies the global mean heat balance. Meanwhile, *Deng and Ridley* [2007] demonstrate that quantification of Joule Heating might be underestimated (in the context of Earth) by models that do not employ vertical momentum calculations. At Titan, we find that the vertical velocities play a critical role in the mass and energy balance in the atmosphere (see Figure 5).

2.1. Constituents in T-GITM Specific to Titan

[11] Although the Titan GITM inherits its numerical fluid solvers directly from its Earth predecessor, it differs greatly in its chemical constituents. The model is composed of 15 neutral species, 5 ionic species, and an electron population equal to the total ion density. The first class of neutral constituents consists of 10 primary species that each possess their own continuity and momentum equations (N_2, CH_4, ^{40}Ar, HCN, H_2, $^{13}CH_4$, ^{15}N-^{14}N, $N(^4S)$, H, and C_2H_4). These species represent constituents that function as (1) key radiatively active neutrals (HCN), (2) major atmospheric constituents by number mixing ratio (N_2, CH_4, H_2), (3) independent constraints to the dynamics of Titan (^{40}Ar, $^{13}CH_4$, ^{15}N-^{14}N), or (4) constituents critical to the chemical formation of HCN ($N(^4S)$, H). We include C_2H_4 in this category also because it possesses no chemical loss terms and thus represents a long-lived species.

[12] The 5 remaining neutral species ($^3CH_2$, $^1CH_2$, CH_3, CH, and H_2CN), the class 2 neutrals, function primarily as components to the chemical scheme currently employed in the model. In order to function as efficiently as possible, the class 2 neutrals are not advected with the mean flow. That is, they only respond to chemical sources and sinks. This approximation does not impact simulated HCN abundances by more than 5%.

[13] The 5 ionic species in T-GITM (N_2^+, N^+, $HCNH^+$, CH_3^+, and $C_2H_5^+$) possess individual continuity equations, and advect according to *Ridley et al.* [2006]. In this approximation, a mean ion-neutral collision frequency $\nu_{in} \sim 10^{-9}$ s^{-1} is employed. In the future, we intend to improve these collision frequencies. However, in this work, we concern ourselves primarily with the neutral atmosphere, and we defer a more complete ion treatment to future publications. Finally, the electrons provide neutrality to the ionosphere and there is currently no separate calculation for electron temperature, velocities, or densities. Overall, these approximations for ion advection and electron temperature do not significantly impact the results for the current neutral atmosphere study.

2.2. Equations of the Titan Global Ionosphere-Thermosphere Model

[14] The Titan GITM model can run in a 1-D configuration, whereby all horizontal transport mechanisms are neglected and only the radial components of the Navier-Stokes equations are retained. This allows for higher-resolution simulations (radially) that are more computationally efficient than the full three-dimensional (3-D) mode. T-GITM revolves during its 1-D mode, allowing the model to simulate a single radial column at the user-specified latitude and longitude

location. In this section, we present a cursory examination of the fluid equations solved by the Titan Global Ionosphere-Thermosphere Model, while appendices A and B contain more details.

2.3. Navier-Stokes Equations

[15] The Titan GITM solves the coupled, nonlinear Navier-Stokes equations, which represent the collision-dominated limit of the 13-moment approximation to the Boltzmann equation [*Schunk*, 1975; *Schunk and Nagy*, 2000]. The model assumes that each neutral species possesses its own continuity equation and its own radial momentum equation. However, T-GITM assumes that all neutral species share the same background temperature [*Ridley et al.*, 2006].

[16] As in the work of *Schunk and Nagy* [2000] and *Gombosi* [1999] the continuity equation is

$$\frac{\partial n_s}{\partial t} + \nabla \cdot (n_s \mathbf{u}_s) = P_s - L_s, \tag{1}$$

where n_s represents the number density (m^{-3}) of species "s", $\mathbf{u}_s$ represents the species-specific velocity $(m\ s^{-1})$, P_s the chemical sources $(m^{-3}\ s^{-1})$, and finally L_s the chemical losses $(m^{-3}\ s^{-1})$. Next, the momentum equation is given by

$$\rho_s \frac{\partial \mathbf{u}_s}{\partial t} + \rho_s \mathbf{u}_s \cdot \nabla \mathbf{u}_s + \nabla p_s + \nabla \cdot \boldsymbol{\tau_s} - \rho_s \mathbf{g}$$
$$+ \rho_s [2\boldsymbol{\Omega}_r \times \mathbf{u}_s + \boldsymbol{\Omega}_r \times (\boldsymbol{\Omega}_r \times r)]$$
$$= \sum_{t \neq s} \rho_s \nu_{st}(\mathbf{u}_t - \mathbf{u}_s) + \sum_{t \neq s} \rho_s \nu_{st}(\boldsymbol{\omega}_s - \boldsymbol{\omega}_t). \tag{2}$$

[17] In equation (2), ρ_s is the mass density $(kg\ m^{-3})$, τ_s the velocity stress tensor (in Pa), $\mathbf{g}$ the gravitational acceleration (in $m\ s^{-2}$), $\boldsymbol{\Omega}_r$ Titan's rotational angular velocity (rads s^{-1}), ν_{st} the momentum collision frequency (s^{-1}), and ω_s the eddy diffusion velocity (in $m\ s^{-1}$). The inclusion of turbulence contributions directly in the radial momentum equation represents a key innovation of this framework, and it is similar to that of *Boqueho and Blelly* [2005]. However, the exact formulation of turbulence employed here possesses several qualities that make it unique from previous methods. More details are provided in Appendix B.

[18] Finally, the energy equation solved by T-GITM is given by

$$\frac{\partial T}{\partial t} + \mathbf{u} \cdot \nabla T + (\gamma - 1)T(\nabla \cdot \mathbf{u}) + \frac{\tau : \nabla \mathbf{u}}{\rho c_v}$$
$$= \frac{1}{\rho c_v}(Q_{EUV} - Q_{HCN} - \nabla \cdot \mathbf{q}). \tag{3}$$

In this expression, T represents the bulk background temperature (K), $\mathbf{u}$ the mass-weighted bulk velocity, τ the bulk velocity stress tensor, ρ the bulk mass density, c_v the specific heat at a constant volume $(J\ (kg\ K)^{-1})$, Q_{EUV} the forcing by the solar Extreme Ultraviolet/Ultraviolet (EUV/UV), Q_{HCN} the HCN rotational cooling, and $\mathbf{q}$ the heat flux. As indicated in the energy equation above, T-GITM assumes that all species possess the same temperature, consistent with the collision-dominated form of the 13-moment equations. Moreover, it employs the collision-dominated form for the

stress tensor and the familiar Fourier's law for the heat flux vector, given by

$$\tau_s = \eta_s \left[\nabla \mathbf{u}_s + (\nabla \mathbf{u}_s)^T - \frac{2}{3}(\nabla \cdot \mathbf{u}_s)I \right], \tag{4}$$

$$\mathbf{q} = -\lambda \nabla T, \tag{5}$$

where λ is the thermal conduction coefficient $(W\ (m\ K)^{-1})$, η_s is the viscosity coefficient $(kg\ m^{-1}\ s^{-1})$, and I is the second-order unit tensor.

[19] As discussed by *Schunk* [1975] and again more recently by *Boqueho and Blelly* [2005], these formulations fail to describe viscosity and thermal conduction near and above the classical exobase. This failure occurs because, near the exobase, the atmosphere is transitioning from a collisional regime to a quasi-collisionless regime, making the collision-dominated forms for the stress tensor and heat vector in equations (4) and (5) unapplicable. Despite the known limitations, we utilize these collisional approximations up to 1500 km, which is roughly coincident with the nominal exobase of N_2. However, because we employ the collision-dominated form of the 13-moment equations, our results may not be strictly valid above 1400 km [*Schunk*, 1975; *Boqueho and Blelly*, 2005].

2.4. Solar EUV/UV Heating Calculations

[20] Solar insolation represents a primary driver for Titan's ionosphere-thermosphere system. T-GITM includes two models for solar irradiance calculations: (1) the formulation of *Hinteregger et al.* [1981] (SERF1) and (2) the *Tobiska* [1991] update to the *Tobiska and Barth* [1990] (SERF2) model. Both models employ the daily average and the 81 day mean of the $F_{10.7cm}$ radio flux. Furthermore, these models are modified to output the solar flux in 55 wavelength bins, spanning 16–1750 Å, that are then used in combination with N_2 and CH_4 photoabsorption and photoionization cross sections. The N_2 photoabsorption cross sections and associated quantum yields are adapted from *Torr et al.* [1979]. Likewise, the CH_4 photoabsorption cross sections and quantum yields are taken from *Schunk and Nagy* [2000].

[21] The solar fluxes at all wavelengths are taken as Earth values at 1 AU and subsequently scaled for Titan's orbit at roughly 9.5 AU. The model accounts for changes in Titan's orbital position and the associated subsolar latitude self-consistently over time, allowing for a realistic evolution of solar insolation as the Kronian system orbits the sun. The ephemeris calculated by the Titan model agrees to within ~1% of the values provided by the NASA/JPL Navigational and Anciliary Information Facility (NAIF) SPICE package for the Saturn-sun distance, the orbital angle, and the subsolar latitude of Titan over the course of a simulated Earth year. The method for calculating the Chapman Integrals of *Smith and Smith* [1972] is used to determine the intensity of incident solar radiation as a function of (1) the different solar wavelengths, (2) the solar zenith angle, and (3) altitude (radial distance). T-GITM then utilizes the Beer-Lambert law to specify how the intensity attenuates as a function of wavelength and altitude. We employ a heating efficiency derived from the work of *De La Haye et al.* [2008a] as a function of

Table 1. Photochemical Reactions in T-GITM

Reaction Number	Photochemical and Electron-Impact Reaction
1	$N_2 + h\nu,\ e^- \rightarrow N(^4S) + N(^2D)$
2	$N_2 + h\nu,\ e^- \rightarrow N(^4S) + N^+$
3	$N_2 + h\nu,\ e^- \rightarrow N_2^+$
4	$CH_4 + h\nu, \rightarrow CH + H_2 + H$
5	$CH_4 + h\nu, \rightarrow {}^3CH_2 + 2H$
6	$CH_4 + h\nu, \rightarrow {}^1CH_2 + H_2$
7	$CH_4 + h\nu, \rightarrow CH_3 + H$
8	$CH_4 + h\nu,\ e^- \rightarrow CH_3^+ + H$

altitude. This heating efficiency is derived from the detailed two-stream suprathermal electron code of *De La Haye et al.* [2007a, 2007b, 2008b] and includes exothermic chemical sources.

2.5. HCN Rotational Cooling Calculations

[22] Hydrogen Cyanide (HCN) represents the primary radiative coolant in Titan's upper atmosphere that balances solar insolation. HCN possesses a permanent dipole moment, allowing for a substantial rotational spectrum. In particular, the rotational lines between the ground and the first excited vibrational states represent a population of 116 well separated molecular lines that remain in approximately local thermodynamic equilibrium (LTE) for the conditions prevailing in Titan's upper atmosphere. Because these molecular lines are well separated, the Titan model can make use of an efficient, full line-by-line algorithm to calculate the radiative transfer of HCN rotational cooling. In order to do this, T-GITM adopts the formulation for HCN rotational cooling developed by *Yelle* [1991] and utilized by *Müller-Wodarg et al.* [2000], where the radiative cooling rates are given by

$$h(z) = 2\pi n_{HCN}(z) \sum_{j=1}^{nlines}$$

$$\cdot \left[\int_{\Delta\nu_j} S_{\nu,\nu_j}(z) \phi_{\nu,\nu_j}(z) \left[C(\tau(z),\nu,\nu_j) \right] \right] d\nu + 2\pi n_{HCN}(z)$$

$$\cdot \sum_{j=1}^{nlines} \left[\int_{\Delta\nu_j} S_{\nu,\nu_j}(z) \phi_{\nu,\nu_j}(z) \left[H_1(\tau(z),\nu,\nu_j) + H_2(\tau(z),\nu,\nu_j) \right] \right] d\nu.$$

In this expression, the three primary radiative transfer terms in the integrand, C, H_1, and H_2 break down as follows: (1) $C(\tau(z),\nu,\nu_j) = -2B_\nu(\tau(z))$ is the isotropic radiation emitted from an altitude "z" in all directions. (2) $H_1(\tau(z),\nu,\nu_j) = B_\nu(0)E_2(\tau_{max} - \tau(z))$ represents the upwelling radiation from the lower boundary that is absorbed by the atmosphere at an altitude level "z". (3) $H_2(\tau(z),\nu,\nu_j) = \int_{\tau(z)}^{\tau_{max}} B_\nu E_1(\tau(z') - \tau(z))d\tau' + \int_0^{\tau(z)} B_\nu E_1(\tau(z) - \tau(z'))d\tau'$ represents the re-absorbed IR radiation incoming to the level "z" from all other altitude levels in the atmosphere.

[23] In this formulation, $\tau(z)$ represents the optical depth of the atmosphere at an altitude level "z," where τ ranges from 0.0 at the top of the atmosphere and reaches the maximum value, τ_{max}, at the lowest-altitude layer in the model [*Chandrasekhar*, 1960; *Goody and Yung*, 1989; *Houghton*, 2002; *Mihalas*, 1978]. B_ν is the Planck function that represents the radiative source function because the rotational lines of HCN are in LTE. E_2 and E_1 represent the first and second exponential integral functions [*Lindfield and Penny*,

1999; *Press et al.*, 1992, 1996; *Ralston and Rabinowitz*, 1978]. $\phi_{\nu,\nu_j}(z)$ represents the line shape, which is taken to be a voigt-broadened line shape [*Fels and Schwarzkopf*, 1981; *Humlícek*, 1982; *Kuntz*, 1997; *Lether and Wenston*, 1991; *Shippony and Read*, 1993; *Thompson*, 1993], and S_{ν,ν_j} represents the rotational line intensity taken from the high-resolution transmission molecular absorption (HITRAN) database [see *Rothman et al.*, 2003, 1998].

[24] HCN rotational cooling is calculated with a full line-by-line calculation over all 116 ground vibrational state rotational lines using a direct integration Gaussian Quadrature technique [*Boughner*, 1985; *Sparks*, 1997]. The HCN rotational cooling is calculated on a plane-parallel grid, which remains potentially inconsistent with both the spherical nature of the real Titan atmosphere and the spherical nature of the T-GITM model. However, true spherical radiative transfer represents an inherently difficult process, both from a theoretical and computational standpoint [*Martin et al.*, 1984; *Rogers and Martin*, 1986, 1984; *Peraiah*, 2001]. Fortunately, as discussed by *Yelle* [1991], the much less computationally and theoretically difficult plane-parallel formulation should still be applicable for energy balance calculations at Titan, despite the potential impacts of curvature at high altitudes.

2.6. Chemistry

[25] T-GITM currently employs a subset of the chemistry found in the detailed 1-D model of *De La Haye et al.* [2008b], identified as Scheme I. This chemical scheme begins with the photodissociation and photoionization of N_2 and CH_4 into the following: H, H_2, $^3CH_2$, $^1CH_2$, CH_3, CH, CH_3^+, N^+, $N(^4S)$, and N_2^+ (see Table 1). These primary fragments then react with one another to produce a second sequence of chemical constituents: H_2CN, $HCNH^+$, C_2H_4, $C_2H_5^+$, and finally HCN. Figure 1 illustrates graphically how the various species in T-GITM interact chemically. Furthermore, Table 2 contains the various bimolecular chemical kinetic rates and reactions currently employed in the model. The electron recombination reactions require an electron temperature in order to calculate a proper reaction rate. Since the Titan model does not currently calculate a separate electron temperature, it employs the measured electron temperature from the Cassini Radio and Plasma Wave Science (RPWS) Instrument [*Wahlund et al.*, 2005]. Thus, while this chemistry is not exhaustive, it produces key thermally active species, HCN, and the major ions, $HCNH^+$ and $C_2H_5^+$, in the upper atmosphere.

2.7. Boundary Conditions and Settings for T-GITM
2.7.1. How We Set Boundary Conditions

[26] The Titan GITM requires the specification of boundary conditions at 500 km (the lower boundary) and at 1500 km (the upper boundary). T-GITM uses two layers of ghost cells on all of its boundaries (both vertical and horizontal). These ghost cells reside outside the computational domain and are where the boundary conditions are imposed. Furthermore, two layers of ghost cells allow the model to calculate derivatives with second-order accuracy at the edges of the physical domain [see *Ridley et al.*, 2006].

[27] In the ghost cells below 500 km, we specify the densities (or equivalently, the mixing ratios) for each of the species included in the model. We also specify the temperatures and vertical velocities at 500 km as follows: (1) $N = N_0$ and $\chi_s = \chi_{s,0}$, (2) $T = T_0$, and (3) $V_s = 0.0$.
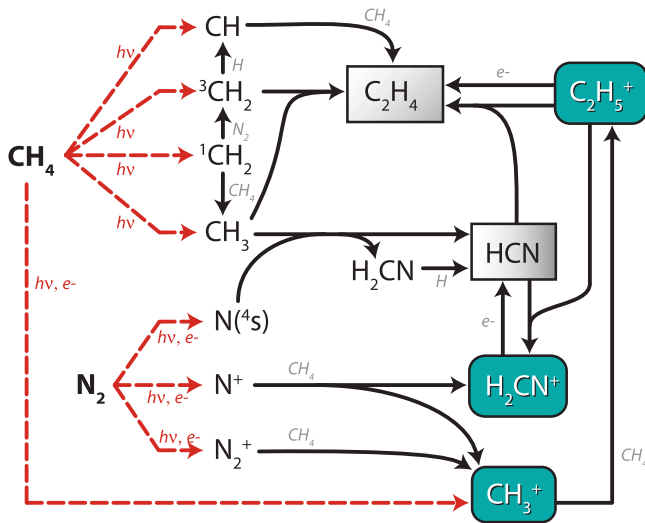
Figure 1. Schematic of the major chemical pathways in T-GITM. This is a subset of chemistry from *De La Haye et al.* [2008b]. In this scheme, N_2 and CH_4 (far left), represent photochemical sources for all subsequent chemistry. Intermediate photochemical products are also shown connected via the red lines. The green species represent the terminal ion products of the subsequent ion-neutral chemistry, including the major ions $C_2H_5^+$ and $HCNH^+$. Finally, two key species are highlighted in gray, C_2H_4 and HCN, the latter of which represents the primary radiative cooling agent in the upper atmosphere.

[28] In these expressions, N is the total density (in m^{-3}), χ_s is the mixing ratio for the individual species, T is the temperature (in K), and V_s is the vertical (radial) velocity (in $m\ s^{-1}$). We assume that these fields remain constant over the course of the simulation. At 500 km, we adopt boundary conditions for densities (mixing ratios) and temperatures that best reflect recent data analysis efforts from Cassini instruments or, when there are no available constraints, results from photochemical models.

[29] At the model's upper boundary (1500 km), we impose the following boundary conditions: (1) $\frac{1}{n_s}\frac{\partial n_s}{\partial r} = -\frac{1}{H_s}$, (2) $\frac{\partial T}{\partial r} = 0.0$, and (3) $\frac{\partial V_s}{\partial r} = 0.0$ or $V_s = V_{escape}$. Thus, at 1500 km, we impose diffusive equilibrium on the neutral densities, which may not be appropriate for escaping species such as H_2. We also assume that the temperature gradient is 0.0 at 1500 km. Finally, we may either adopt a zero vertical velocity gradient, or we can impose an escape velocity, when it is needed. By setting $V_s = V_{escape}$ we are enforcing an external escape process upon the model that will feed back into the velocities below the boundary. In doing so, we are implying an external driver for the escape process. A well-known instance of this is classical Jeans escape, which is not contained explicitly in the Navier-Stokes equations and must be imposed at the top of the model to simulate escape of particles from the exosphere.

2.7.2. Settings for the Simulations

[30] Settings for all of the simulations were specified to be consistent with the mean conditions on Titan between TA and T40 [see *Müller-Wodarg et al.*, 2008]. The solar activity level was set to $F_{10.7cm} = 80.0 \times 10^{-22}\ W\ m^{-2}\ Hz^{-1}$. All solar fluxes were taken as values at 1 AU and scaled for the

Titan-solar distance. The 1-D T-GITM model was set to 45° N latitude, consistent with the mean latitude sampled by INMS between TA and T40. We adopt a nonuniform radial grid that possesses a 2.5 km vertical spacing at 500 km and rises to a uniform 10 km spacing above 600 km. This allows us to better resolve the region near the lower boundary while not sacrificing computational time by having a uniform resolution of 2.5 km throughout the entire calculation domain. T-GITM can readily accommodate such nonuniform grids (both radial and horizontal) self-consistently in the fluid solvers [cf. *Ridley et al.*, 2006].

[31] At 500 km (the lower boundary of T-GITM), densities and mixing ratios for all constituents are fixed and the values for the major species are listed for each simulation in Table 3. The total density at 500 km can be directly derived by integrating from 0 km to 500 km using the hydrostatic relation [*Schunk and Nagy*, 2000, equation 10.63] and the nominal temperature derived from the Composite Infrared Spectrometer (CIRS) instrument [*Achterberg et al.*, 2008; *Teanby et al.*, 2007] in the lower atmosphere. The total density derived from this method at 45°N latitude is $7.37 \times 10^{19}\ m^{-3}$. However, this value is very sensitive to the assumed temperature structure and, by decreasing the mean temperature in the lower atmosphere by 5%, the densities at 500 km can be reduced by ~35% to $4.80 \times 10^{19}\ m^{-3}$. In addition to density variability, we assume a 20 K uncertainty in the lower boundary temperatures at 500 km, spanning the range from 160 K to 180 K, consistent with the range of temperatures in the lower atmosphere reported by *Achterberg et al.* [2008].

[32] Along with the total density, the mixing ratios for all species are also specified at 500 km. The methane volume mixing ratio is set to $1.23 \pm 0.07\%$, which is consistent with *Strobel* [2009] (1.23%), and with measurements by CIRS, $1.6 \pm 0.5\%$, [*Flasar et al.*, 2005], but lower than measurements by the Gas Chromatograph Mass Spectrometer (GCMS), $1.4 \pm 0.07\%$ [*Niemann et al.*, 2005]. H_2 mixing ratios at 500 km are set between 0.32 and 0.35%, which is consistent with *Yelle et al.* [2006] ($4.0 \pm 1.0 \times 10^{-3}$) but are

Table 2. Intermolecular Chemical Reactions and Associated Rates in T-GITM[a]

Reaction Number	Chemical Reaction	Reaction Rate ($m^3\ s^{-1}$)
	Neutral Bimolecular Chemistry	
1	$^3CH_2 + H \rightarrow H_2 + CH$	$4.70 \times 10^{-16}\ e^{-370.0/T}$
2	$CH_3 + {}^3CH_2 \rightarrow C_2H_4 + H$	7.00×10^{-17}
3	$CH_4 + CH \rightarrow C_2H_4 + H$	$3.96 \times 10^{-14}\ T^{-1.04}\ e^{-36.1/T}$
4	$CH_4 + {}^1CH_2 \rightarrow CH_3 + CH_3$	6.00×10^{-17}
5	$N(^4S) + CH_3 \rightarrow H_2CN + H$	5.76×10^{-17}
6	$N(^4S) + CH_3 \rightarrow HCN + H_2$	6.00×10^{-18}
7	$N_2 + {}^1CH_2 \rightarrow {}^3CH_2 + N_2$	$2.36 \times 10^{-20}\ T$
8	$H_2CN + H \rightarrow HCN + H_2$	7.00×10^{-17}
	Ion-Neutral Chemistry	
9	$CH_3^+ + CH_4 \rightarrow C_2H_5^+ + H_2$	$1.10 \times 10^{-15} \pm 20\%$
10	$C_2H_5^+ + HCN \rightarrow HCNH^+ + C_2H_4$	$2.70 \times 10^{-15} \pm 20\%$
11	$N^+ + CH_4 \rightarrow CH_3^+ + NH$	$5.75 \times 10^{-16} \pm 15\%$
12	$N^+ + CH_4 \rightarrow HCNH^+ + H_2$	$4.14 \times 10^{-16} \pm 15\%$
13	$N_2^+ + CH_4 \rightarrow CH_3^+ + N_2 + H$	$9.804 \times 10^{-16} \pm 15\%$
	Electron Recombination Chemistry	
14	$C_2H_5^+ + e^- \rightarrow C_2H_4 + H$	$7.2 \times 10^{-14}\ (300.0/T_e)^{0.5}$
15	$HCNH^+ + e^- \rightarrow HCN + H$	$6.40 \times 10^{-13}\ (300.0/T_e)^{0.5}$

[a]*De La Haye et al.* [2008b], *Wilson* [2002], and *Wilson and Atreya* [2004].

Table 3. Key T-GITM Parameter Settings at 500 km and 1500 km[a]

	Lower Boundary at 500 km					Topside Boundary at 1500 km			Turbulence	
	Total Density (molecules m^{-3})	T (K)	CH$_4$ Mixing Ratio	H$_2$ Mixing Ratio	^{40}Ar Mixing Ratio	Φ_{CH_4} (molecules m^{-2} s^{-1})	Φ_{H_2} (molecules m^{-2} s^{-1})	Q_{plasma} (eV cm^{-3} s^{-1})	K$_0$ (m^2 s^{-1})	K$_\infty$ (m^2 s^{-1})
Model 1	4.80×10^{19}	160	1.23×10^{-2}	3.2×10^{-3}	4.15×10^{-5}	1.64×10^{13}	1.02×10^{14}	150.0	932.0	3200.0
Model 2	4.80×10^{19}	160	1.23×10^{-2}	3.2×10^{-3}	4.15×10^{-5}	1.28×10^{13}	9.20×10^{13}	0.0	932.0	3200.0
Model 3	4.80×10^{19}	160	1.23×10^{-2}	3.2×10^{-3}	4.15×10^{-5}	1.86×10^{13}	1.06×10^{14}	0.0	932.0	3200.0
Model 3(NC)	4.80×10^{19}	160	1.16×10^{-2}	3.2×10^{-3}	4.15×10^{-5}	2.64×10^{13}	1.02×10^{14}	20.0	932.0	3200.0
Strobel [2009] (Figure 6)	$\sim1.21 \times 10^{20}$	~140	1.25×10^{-2}	2.9×10^{-3}	2.9×10^{-5}	2.04×10^{13}	1.1×10^{14}	0.0	3.0×10^3	2.0×10^4
Yelle et al. [2008]	$\sim6.20 \times 10^{19}$	~180–185	1.1×10^{-2}	N/A	4.30×10^{-5}	2.5–3.0×10^{13}	N/A	0.0	3.0×10^{-2}	3000.0

[a]The topside escape fluxes, Φ_{CH_4}, and Φ_{H_2} are referred to the surface. K$_0$ and K$_\infty$ represent the components of the eddy diffusion coefficient. We also include settings from *Strobel* [2009, Figure 6] and from *Yelle et al.* [2008].

higher than values predicted by *Krasnopolsky* [2009] and *Lebonnois et al.* [2003] at 500 km. The radiogenic ^{40}Ar number mixing ratio is set to 4.114×10^{-5}, which is consistent with the measurements of GCMS [*Niemann et al.*, 2005] ($4.32 \pm 0.1 \times 10^{-5}$) when extended upward from the surface to 500 km, allowing for very slight diffusive separation.

[33] The thermally active neutral constituent, HCN, is set to a volume mixing ratio of 2.5×10^{-6}. This is consistent with the range of mixing ratios derived from CIRS measurements near 500 km [*Teanby et al.*, 2007], which range between $\sim1.0 \times 10^{-6}$ and $\sim1.0 \times 10^{-5}$. We note that, since HCN is produced in the thermosphere and is transported into the lower atmosphere, a fixed mixing ratio boundary condition may artificially maintain higher HCN mixing ratios near the lower boundary. However, recent work by *Krasnopolsky* [2009] indicates that significant HCN chemistry occurs between 100 and 400 km, which is currently not modeled by T-GITM. Since we cannot self-consistently model the chemistry occurring below 500 km (and the resulting impacts to the mixing ratio at 500 km), we choose to fix the boundary condition for HCN consistent with the best available data from CIRS. Last, C$_2$H$_4$ is currently set to a mixing ratio of 3.0×10^{-6} at 500 km, consistent with the photochemical work by *De La Haye et al.* [2008b] and *Lebonnois et al.* [2003]. For all other species, which represent the photochemically produced ion and neutral species, mixing ratios of 10^{-15} are employed at the lower boundary. We note that changing the mixing ratios of these photochemical species does not appreciably impact their calculated densities in the upper atmosphere above 600 km.

2.8. Constraining Turbulence Using ^{40}Ar

[34] Subgrid (i.e., nonresolved) turbulence and its various formulations represent heuristic adjustments to the Navier-Stokes fluid equations. Hence, the only true test for a given formulation of turbulence is best observed by its impacts upon an inert tracer species. In Titan's upper atmosphere, the radiogenic isotope ^{40}Ar represents a prime candidate for such a test, since it is measured in the upper atmosphere and remains chemically inert. Thus, as is done by *Yelle et al.* [2008], we utilize the inert neutral gas ^{40}Ar to constrain the eddy diffusion coefficient in T-GITM.

[35] For the purposes of this calibration study, we rely upon a single formulation for turbulent mixing in the upper atmosphere of Titan, which is consistent with that proposed by *Yelle et al.* [2008] and is given by

$$K(r) = \frac{K_0 K_\infty (p_0/p(r))^\gamma}{K_0 (p_0/p(r))^\gamma + K_\infty}, \tag{6}$$

where $K_0 = 3.0 \times 10^{-2}$ m^2 s^{-1}, $p_0 = 0.15$ dyne cm^{-2}, $K_\infty = 3200.0$ m^2 s^{-1}, and $\gamma = 0.90$. *Yelle et al.* [2008] indicates that this formulation is consistent with photochemical modeling constraints in the lower atmosphere, such as *Vuitton et al.* [2008].

3. Scientific Results

3.1. Method of Data Comparison

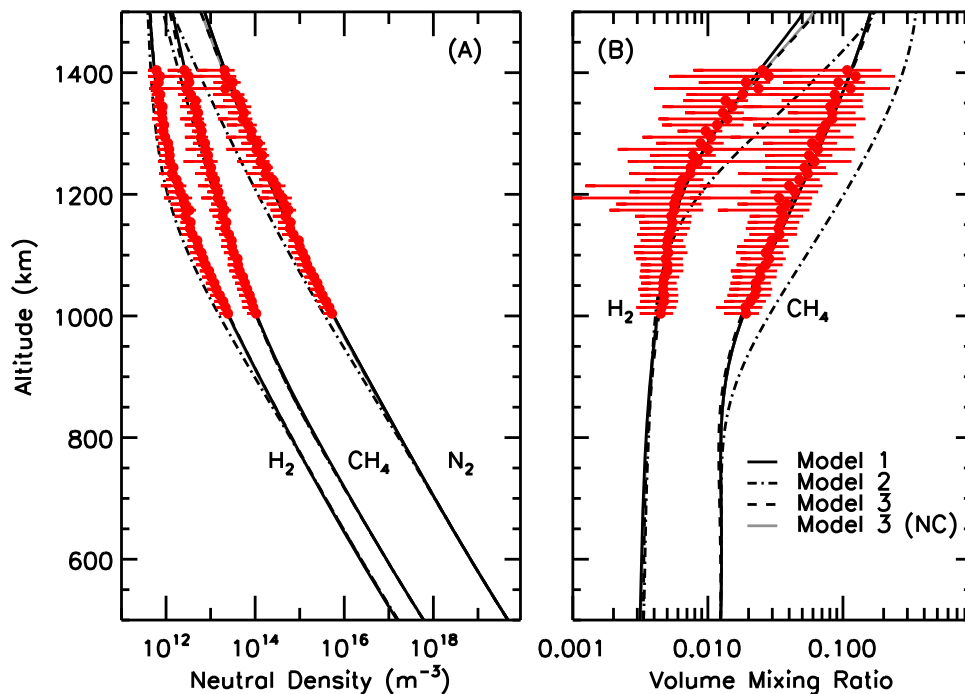[36] The INMS data set samples a wide range of longitudes, latitudes, and times, making a comparison with a 1-D

Figure 2. (a) T-GITM neutral densities (black lines) of N_2, CH_4, and H_2 are compared against the INMS-derived neutral densities of *Magee et al.* [2009] shown as red circles. (b)The mixing ratios of CH_4 and H_2 are similarly compared against the data. A detailed data-to-model analysis is provided in Table 4.

model difficult. In order to better constrain the T-GITM simulations of this section with data, an average INMS altitude profile is utilized. All ingress neutral density data from flybys TA through T40 (17 total flyby passes) are binned in 10 km increments, but we exclude egress data in order to alleviate any potential impacts of adsorbed species in the INMS instrument [see *Magee et al.*, 2009]. Next, this binned data is then averaged into a single altitude profile, which can be compared against 1-D T-GITM simulations. The uncertainties (horizontal red bars in Figure 2) depicted in the INMS profiles of this study are due to geophysical variances in the atmosphere of Titan itself, rather than counting statistics and/or systematic errors. The counting statistical errors for N_2, CH_4, and H_2 are significantly less than the geophysical uncertainties and they would not be visible in the results presented here.

[37] An iterative process for reproducing the averaged ingress INMS data of *Magee et al.* [2009] is followed for every simulation. The steps are delineated as follows: (1) Total densities and temperatures were adjusted at 500 km in order to best fit N_2 measurements between 900 km and 1000 km. (2) The topside external energy deposition into the upper atmosphere was adjusted to best fit the measured INMS N_2 densities between 1200 km and 1500 km. (3) The eddy diffusion coefficient at 500 km and the maximum value of the eddy diffusion coefficient were adjusted to best fit the ^{40}Ar mixing ratios. (4) When necessary, the velocities at 1500 km for CH_4 and H_2 were adjusted in order to best match their INMS mixing ratios.

[38] The external heating in step 2 above can be composed of several processes, among which we include (1) horizontal transport of energy from the summer (southern) hemisphere

to the northern (winter) hemisphere not modeled by the 1-D framework, (2) exospheric heat sources [e.g., *Shah et al.*, 2009; *Sillanpää et al.*, 2007; *Smith et al.*, 2009], and (3) wave heating sources [*Strobel*, 2006]. Recent work in a 3-D version of T-GITM indicates that horizontal transport plays an important role in the energetic balance in the northern hemisphere [*Bell et al.*, 2009]. However, for the purposes of this work, we refer to a generalized heat flux incident on the topside boundary of the model. The reader should regard the external heating required by the 1-D model in this investigation as an upper limit on the necessary exospheric/plasma heating required by the T-GITM framework to reproduce the INMS measurements.

[39] When comparing the model simulations with the INMS data, we calculate percentage deviations between the model and the averaged ingress INMS data according to the following formula:

$$\%Deviation = \sum_{i=1}^{N} \frac{|Model(i) - Data(i)|}{Data(i)}, \quad (7)$$

where the sum is over all the individual data points. Thus, these deviations quantify how well the T-GITM model compares to the entire altitude profile of the selected field (i.e., density or mixing ratio). These errors are presented in Table 4. In order to provide a fiducial for comparison, we also show the percentage deviations between a nonlinear least squares fit to the data and the averaged INMS ingress data.

3.2. Calibration Benchmark Runs

[40] In this section, we present a series of T-GITM simulations using parameter constraints consistent with the

Table 4. Percent Deviations Between T-GITM Simulated Fields and the INMS Measurements of *Magee et al.* [2009][a]

	N_2 Density	CH_4 Density	H_2 Density	CH_4 Mixing Ratio	H_2 Mixing Ratio
Model 1	10.20	5.91	6.87	7.47	6.95
Model 2	57.91	13.91	39.80	123.4	69.7
Model 3	10.30	6.48	7.15	6.28	7.15
Model 3 (NC)	9.62	8.10	7.26	6.51	6.81
Least Squares	7.31	4.74	4.99	4.86	4.77

[a]Percent deviations from a least squares analysis of the data is provided as a fiducial. All errors are in arithmetic % deviations.

collective works of *Cui et al.* [2008], *Strobel* [2008, 2009], and *Yelle et al.* [2008]. We compare these individual simulations to one another, to the INMS data of *Magee et al.* [2009], and to the ⁴⁰Ar data of *Yelle et al.* [2008]. These model runs are labeled models 1, 2, 3, and 3(NC) in Figures 2–3 and in Tables 3–4. Three simulations (models 1–3) employ a common lower boundary methane volume mixing ratio of 1.23% and a common lower boundary molecular hydrogen volume mixing ratio of 3.2×10^{-3}. However, model 3(NC) requires a slightly reduced methane mixing ratio of 1.16%.

[41] Model 1 possesses the full self-consistent HCN chemistry of Figure 1 as well as an additional heating rate at the exobase of 150.0 eV cm^{-3} s^{-1}. Model 2 is identical to model 1, except the exospheric plasma heating rate is removed. In model 3, the HCN volume mixing ratio is artificially constrained to a maximum value of 1.9×10^{-4} at high altitudes, consistent with the works of *Strobel* [2008, 2009] and *Vuitton et al.* [2006]. Finally, model 3(NC) is identical to model 3, except that the chemical losses for CH_4 are ignored, consistent with *Yelle et al.* [2008]. Please note that we still calculate chemical losses for CH_4 to drive the reactions of Figure 1, but we simply do not subtract this chemical loss from the methane. This treatment, while inconsistent, represents the best approximation to the study by *Yelle et al.* [2008], which neglected chemical calculations. All four simulations utilize the eddy diffusion profile suggested by *Yelle et al.* [2008] to best match the ⁴⁰Argon densities derived from the data reduction methods of *Cui et al.* [2009].

[42] The simulated major neutral densities from models 1, 2, 3, and 3(NC) are shown in Figure 2. Figure 2a depicts the
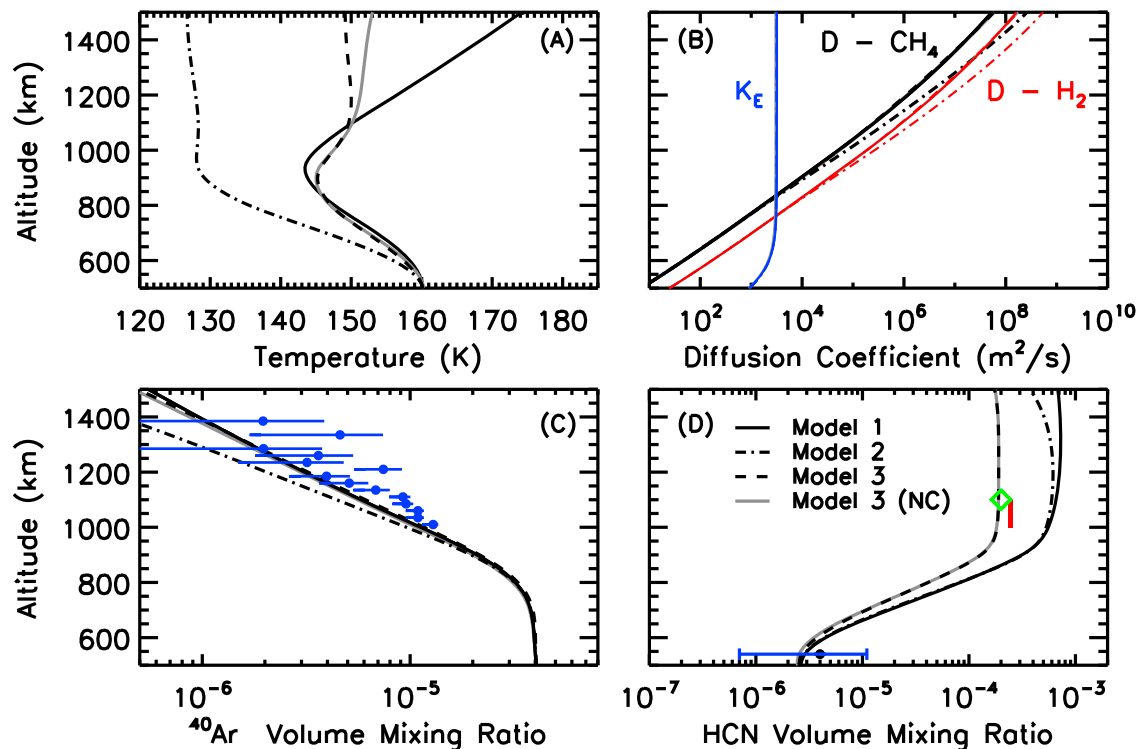

Figure 3. Benchmark test cases for T-GITM. All simulations shown utilize the turbulent coefficient altitude profile of *Yelle et al.* [2008]. Model 1 (solid black line) includes complete self-consistent HCN chemistry shown in Figure 1 and includes external heating at 1500 km. Model 2 (dashed line) is identical to model 1, but it possesses no external heating at 1500 km. Model 3 possesses no external heating and enforces an artificial maximum HCN mixing ratio of 1.9×10^{-4}, which closely matches the modeling results of *Vuitton et al.* [2006] (green diamond in Figure 3d). Model 3(NC), denoted by the gray lines, is identical to model 3, but chemical losses are not subtracted from CH_4.
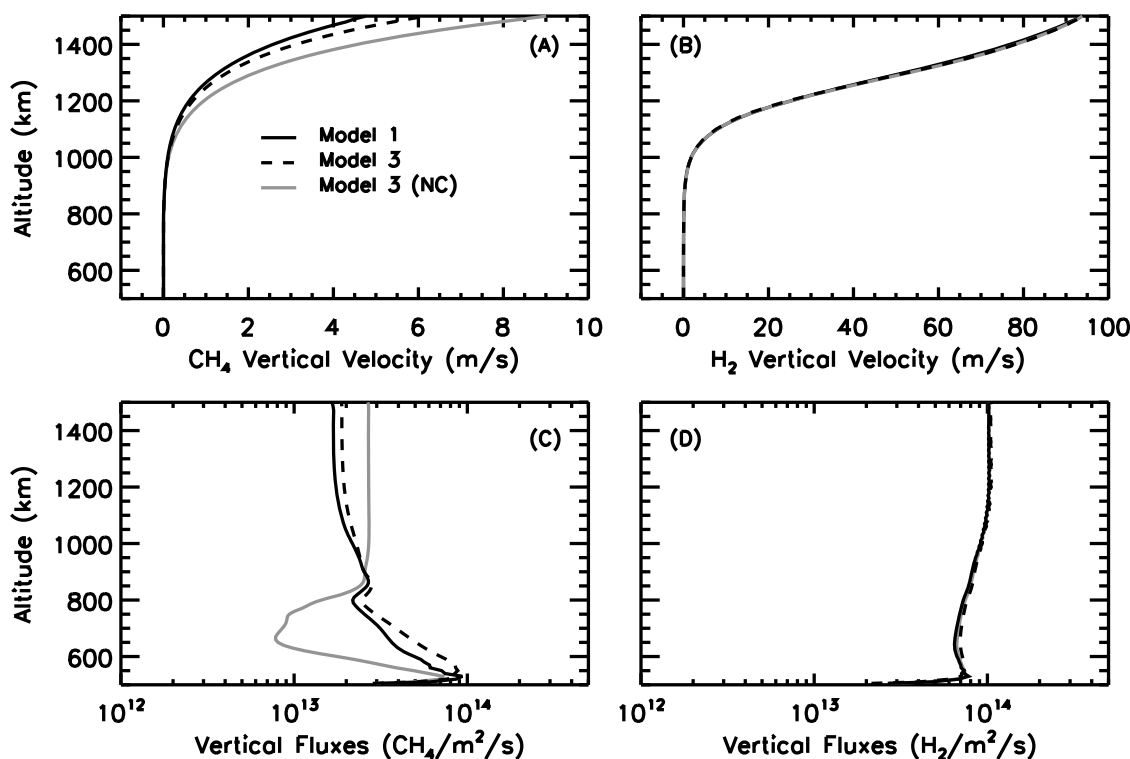
Figure 4. Vertical velocities and fluxes of CH_4 and H_2 from the T-GITM simulations, omitting model 2. (a) The vertical velocities for methane from 500 km to 1500 km; (b) the same for molecular hydrogen. (c) The vertical fluxes for CH_4; (d) the vertical fluxes for H_2 (all fluxes scaled relative to the surface of Titan).

T-GITM simulated (black and gray lines) neutral densities of N_2, CH_4, and H_2, while Figure 2b contains the associated mixing ratios of CH_4 and H_2. Also plotted in Figure 2 are the INMS-measured densities and mixing ratios (red circles). The uncertainty in the densities and mixing ratios are depicted by the horizontal red bars, and they are due to geophysical variations in Titan's upper atmosphere during the time period between TA and T40.

[43] Figure 3a shows the calculated thermal structures for all three models, highlighting the differences between them. Model 2 (Full HCN, no heating) possesses by far the coldest temperatures over most of the atmosphere. The thermal structure of model 1 (Full HCN, external heating) exhibits a positive radial gradient (increasing with altitude) and the highest exobase temperature of 174 K, illustrating the influence of the imposed external heating at the exobase in this simulation. Model 3 (Artificial HCN, no heating) depicts a thermal structure consistent with that of *Yelle et al.* [2008] above 1000 km, with an exobase temperature of 149 K and possessing a slightly negative radial temperature gradient. Model 3(NC) possesses a thermal structure very similar to that of model 3, however it possesses a positive radial gradient and an exobase temperature of roughly 153 K. This is due to the small, but nonnegligible, plasma heating required (see Table 3) to balance the greater adiabatic cooling resulting from the enhanced escape rates of CH_4.

[44] Figure 3b depicts the molecular diffusion coefficients and eddy diffusion coefficients for all four models. The operational location of the turbopause for both CH_4 and H_2 occurs where the molecular and eddy diffusion coefficients

are equal. Since all of the simulations rely upon the same eddy diffusion coefficient, they all possess turbopause altitudes of 840 km for methane and 760 km for molecular hydrogen. Figure 3c depicts the resulting [40]Ar volume mixing ratio profiles using these eddy diffusion coefficients. Plotted in blue are the approximate values of the Argon mixing ratios taken from *Yelle et al.* [2008] and *Cui et al.* [2009]. The simulated profile passes near the two bottom-most data points, consistent with *Yelle et al.* [2008, Figure 4].

[45] Finally, Figure 3d contains the HCN volume mixing ratio profiles for the four simulations (black and gray lines), those derived directly from the INMS data of *Magee et al.* [2009] (red region), and those simulated by the 0-D chemical model of *Vuitton et al.* [2006] (the green diamond). Models 1 and 2 utilize the full chemistry of Figure 1 to calculate the HCN abundances, resulting in much higher mixing ratios than would be expected from data analysis of *Magee et al.* [2009] and from the chemical modeling of *Vuitton et al.* [2006]. Despite this, the values by models 1 and 2 are consistent with the HCN mixing ratios calculated recently by *Krasnopolsky* [2009] using a more exhaustive chemical scheme than that employed by T-GITM. Models 3 and 3(NC) both possess the artificial maximum of 1.9×10^{-4} imposed to be consistent with *Strobel* [2008, 2009] and the modeling work of *Vuitton et al.* [2006].

3.3. Vertical Velocities and Fluxes of CH_4 and H_2

[46] The previous section outlines the simulated composition of four different model configurations and, in this section, we focus on the calculated radial dynamics of three
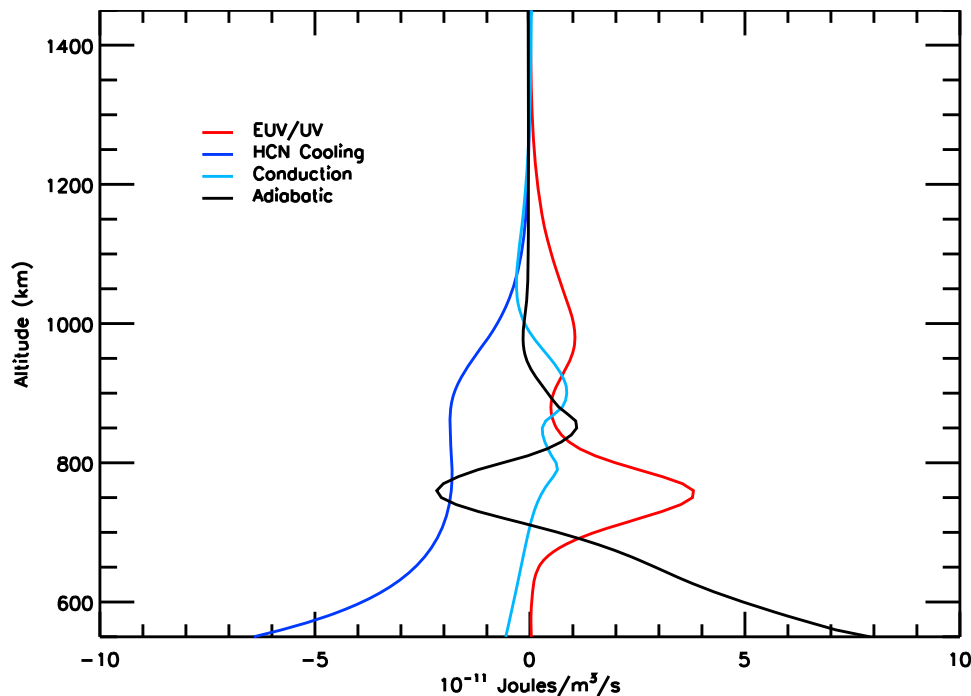
Figure 5. T-GITM thermal balance terms for model 3. The solar EUV/UV heating is shown in red. The HCN rotational cooling is depicted in dark blue. The thermal conduction is shown as the aquamarine (light blue) line. Finally, the adiabatic heating/cooling is the black line. All simulations possess thermal balances very similar to this prototype example.

selected simulations: models 1, 3, and 3(NC). We omit model 2, since it compares poorly with INMS data. Figure 4a contains the vertical velocities of CH_4 and Figure 4b contains the vertical velocities of H_2 for the three simulations. Figures 4c and 4d contain the associated vertical fluxes, scaled so that they are all relative to the surface of Titan. The topside vertical fluxes depicted in Figure 4 for CH_4 and H_2 are listed in Table 3.

[47] First, we note from Figures 4a and 4b that the CH_4 vertical velocities among the three models show a wide variance, while the H_2 vertical velocities remain very consistent. Model 1 possesses the lowest topside escape speeds of methane of 4.5 m s^{-1} and, similarly, the lowest topside escape flux of methane of 1.64×10^{13} CH_4 m^{-2} s^{-1}. Model 3, possesses a higher CH_4 radial velocity of 6.0 m s^{-1} and escape fluxes of 1.86×10^{13} CH_4 m^{-2} s^{-1}. Finally, in model 3(NC), when methane chemical losses are ignored, the model requires the highest vertical speed of 9.0 m s^{-1} and an escape flux of 2.64×10^{13} molecules m^{-2} s^{-1} (compare Table 3).

[48] By contrast, all of the model configurations require roughly the same H_2 escape speeds of 90.0 m s^{-1} and vertical fluxes, ranging between 1.02 and 1.06×10^{14} molecules m^{-2} s^{-1}. In every model configuration, the H_2 fluxes asymptote high in the atmosphere, indicating that they have reached a limiting value, which we interpret as its limiting flux [*Hunten*, 1973]. If we force the model to exceed this limiting flux at 1500 km, then the H_2 mixing ratio drops precipitously at the highest altitudes. This further indicates that H_2 obtains ~99% of its limiting fluxes high in the atmosphere, which is consistent with the work by *Strobel* [2009] and *Cui et al.* [2008].

[49] Finally, we note that the velocities in Figure 4 for both CH_4 and H_2 must be imposed at 1500 km. The model cannot self-consistently calculate these escape speeds. Instead, in order to match the INMS composition measurements for CH_4 and H_2, we must enforce these high escape speeds on T-GITM, implying that the driving force behind these escape speeds lies outside the modeling regime.

3.4. Thermal and Momentum Balances

[50] Figures 5 and 6 contain the thermal and momentum balances, respectively, for model 3. We depict only model 3, since all of the simulations possess very consistent energy and momentum balances, making additional plots redundant to the present discussion. Figure 5 contains the dominant heating and cooling rates for this simulation. The solar EUV/UV heating rates are shown in red, the HCN rotational cooling rates are shown in deep blue, the thermal conduction heating/cooling rates are shown in aquamarine, and Last the adiabatic heating/cooling rates are shown in black. In Figure 5, the HCN cooling rates and the adiabatic heating/cooling dominate the thermal structure in the lowest altitudes. Above 700 km, the solar EUV/UV heating becomes critical. At all altitudes, thermal conduction provides the balance to the heating and cooling rates.

[51] Figures 6a and 6b contain the momentum balances for CH_4 and H_2, respectively, in model 3. The pressure-gravity acceleration is shown plotted in red and given by $-\frac{\nabla P_s}{\rho_s} + g$, whereas the neutral friction and turbulent accelerations are plotted in blue. The pressure-gravity acceleration is by far the dominant driver in the vertical direction.
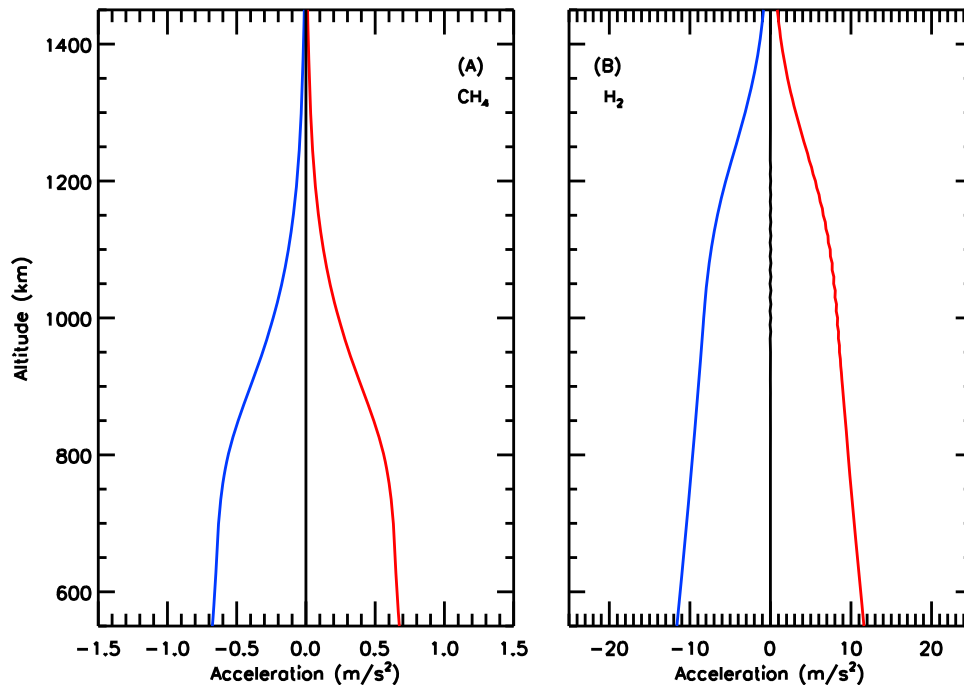
Figure 6. Momentum balance terms (acceleration terms) in model 3. (a) The accelerations for methane. (b) The accelerations for molecular hydrogen. The blue lines are the neutral friction and eddy diffusive accelerations, while the red lines are the upward pressure gradient accelerations. The black line is the summation of these two terms, which is nearly 0.0 over the entire altitude regime.

The neutral friction and turbulent accelerations provide balance to this acceleration, since both accelerations sum to zero at all altitudes (shown by the black line). Figure 6 demonstrates that GITM can calculate nonhydrostatic solutions self-consistently, while also showing that the major momentum terms balance at all altitudes in the computational domain.

4. Discussion and Analysis

[52] As discussed in the introduction, the motivation for this study is twofold: (1) to outline the physics and numerics comprising T-GITM and (2) to validate/benchmark this model with a series of simulations. In order to accomplish the second major goal, we compare the models' simulated densities and mixing ratios against those of INMS, as determined by the methods of *Magee et al.* [2009]. We then compare the calculated topside escape rates of methane and molecular hydrogen from T-GITM with recent estimates by *Cui et al.* [2008], *Strobel* [2009], and *Yelle et al.* [2008].

4.1. T-GITM Compared With INMS Densities and Mixing Ratios

[53] As can be seen in Table 4 and in Figure 2, model 1 (Full HCN, heating), model 3 (Artificial HCN, no heating), and model 3(NC) do an equivalently good job of reproducing the INMS neutral density and mixing ratio measurements, each possessing percentage deviations of less than 10.5% in all of the relevant fields. We also note that models 1, 3, and 3(NC) match the ^{40}Ar mixing ratios of *Yelle et al.* [2008] in a way consistent with that work, which is verified

visually in Figure 3. Moreover, we maintain that models 1, 3, and 3(NC) are indistinguishable from one another based solely upon their percentage deviations from the INMS flyby data of *Magee et al.* [2009]. On the other hand, model 2 (Full HCN, no heating) fails to adequately represent the upper atmosphere in almost every sense, possessing the highest percent deviations of this investigation.

4.2. Calculated Topside Escape Fluxes

[54] While models 1, 3, and 3(NC) match INMS data equivalently well, we next calibrate the predicted topside escape fluxes of hydrogen and methane from Titan Global Ionosphere-Thermosphere Model against those predicted by *Cui et al.* [2009], *Strobel* [2009], and *Yelle et al.* [2008]. We summarize this comparison in Table 5, which highlights the escape fluxes of CH_4, H_2, and the homopause altitudes for models 1, 3, and 3(NC) as well as the relevant results from these previous studies. As shown by Table 5, models 3 and 3(NC) represent the closest approximations to the collective works of *Cui et al.* [2008], *Strobel* [2009], and *Yelle et al.* [2008].

[55] Model 3 requires escape fluxes for CH_4 of $\Phi_{CH_4} = 1.86 \times 10^{13}$ molecules m^{-2} s^{-1} (all fluxes are referred to the surface of Titan, r = 2575 km), agreeing to within 10% with those reported by *Strobel* [2009] (2.04×10^{13} molecules m^{-2} s^{-1}). Also like *Strobel* [2009], model 3 imposes an artificial cap on the HCN volume mixing ratios of roughly 1.9×10^{-4}, requires no plasma heating at 500 km, and matches the ^{40}Ar mixing ratios determined by the methods of *Cui et al.* [2009]. These similarities, as well as the very consistent

Table 5. Comparison of Topside Escape Fluxes of the Current Work With Key Recent Studies

	Φ_{CH_4} (molecules m^{-2} s^{-1})	Φ_{H_2} (molecules m^{-2} s^{-1})	Q_{Plasma} (eV cm^{-3} s^{-1})	Homopause Altitude (km)
Model 1	1.64×10^{13}	1.02×10^{14}	150.0	840.0
Model 2	1.28×10^{13}	9.20×10^{13}	0.0	840.0
Model 3	1.86×10^{13}	1.06×10^{14}	0.0	840.0
Model 3(NC)	2.64×10^{13}	1.02×10^{14}	20.0	840.0
Cui et al. [2008]	N/A	$1.1–1.37 \times 10^{14}$	0.0	N/A
Strobel [2009]	2.04×10^{13}	1.10×10^{14}	0.0	840.0
Yelle et al. [2008]	$2.50–3.0 \times 10^{13}$	N/A	0.0	840.0

estimates for methane escape, suggest that model 3 represents a close analogue to the study of *Strobel* [2009].

[56] Similarly, model 3(NC) requires topside methane escape fluxes of 2.64×10^{13} CH$_4$ m^{-2} s^{-1}, which falls within the range calculated by *Yelle et al.* [2008] ($2.5–3.0 \times 10^{13}$ CH$_4$ m^{-2} s^{-1}). In model 3(NC), we ignore chemical losses for CH$_4$, meaning that more methane is available to escape the topside of Titan. Moreover, this simulation matches the ^{40}Ar volume mixing ratios determined from the analysis methods of *Cui et al.* [2009]. This close correlation suggest that model 3(NC) represents a close approximation to the work by *Yelle et al.* [2008].

[57] Models 1 and 2 possess CH$_4$ topside escape fluxes that differ from those estimated by *Strobel* [2009] and *Yelle et al.* [2008]. Model 2 fails to match the INMS data and it may be ignored for the purposes of comparison. However, model 1 reproduces the major densities and mixing ratios of *Magee et al.* [2009]. Furthermore, it matches the ^{40}Ar mixing ratios of *Yelle et al.* [2008], exhibiting a homopause altitude of 840 km, just as in model 3 and model 3(NC). Despite these similarities, this simulation predicts escape fluxes of methane 20% below those of *Strobel* [2009] and roughly 40% less than the lowest value established by *Yelle et al.* [2008]. We attribute this discrepancy to the increased HCN abundances in the upper atmosphere, which subsequently reduce the energy available for escape and necessitate the significant plasma heating in this case. This result indicates that the process of matching the INMS densities and mixing ratios may not sufficiently constrain the topside escape fluxes, since models 1, 3, and 3(NC) all match the INMS densities and still possess significant differences in their topside escape fluxes.

[58] Unlike the predicted CH$_4$ escape fluxes, models 1, 3, and 3(NC) all simulate very consistent escape fluxes of H$_2$, as shown in Table 5. The simulated H$_2$ escape fluxes for models 3 and 3(NC), $\Phi_{H_2} = 1.06 \times 10^{14}$ molecules m^{-2} s^{-1}, closely match those of *Strobel* [2009], who reported escape fluxes of 1.1×10^{14} H$_2$ m^{-2} s^{-1}, and those of *Cui et al.* [2008], who calculated H$_2$ fluxes between 1.1 and 1.37×10^{14} molecules m^{-2} s^{-1}. Model 1 also predicts H$_2$ escape fluxes consistent with these earlier studies, although they are slightly lower at 1.02×10^{14} molecules m^{-2} s^{-1}. Based upon these simulations, we conclude that the molecular hydrogen escape fluxes, unlike those of CH$_4$, remain very consistent among all of the models mentioned here. This is most likely due to the fact that H$_2$ escape is limited deep in the atmosphere according to its limiting flux [*Hunten*, 1974], and this value seems to be very consistent among all of the studies considered here.

4.3. Mechanisms Driving Escape

[59] A significant problem with all of the simulations of this study is that they cannot self-consistently calculate the escape rates suggested in Tables 3 and 5 from the physics of the Navier-Stokes equations. The escape speeds for CH$_4$ and the associated escape fluxes are much higher than those anticipated from Jeans escape. In order to achieve the escape fluxes reported, we must impose vertical speeds as boundary conditions at 1500 km. If we instead rely only upon the Navier-Stokes equations to calculate the escape speeds, then we cannot match the INMS CH$_4$ measurements with less than 30% deviations. This is consistent with *Yelle et al.* [2008], who finds that they must also enforce high escape fluxes on CH$_4$ in order to reproduce the INMS composition measurements, using the ^{40}Ar mixing ratios derived by the methods of *Cui et al.* [2009]. These results suggest that, when constrained to match the ^{40}Ar mixing ratios presented by *Yelle et al.* [2008], high outflows of methane are required in order to reproduce the INMS densities and mixing ratios of *Magee et al.* [2009]. In other words, enforcing a homopause altitude of 840 km requires high outflows of methane in T-GITM that cannot be self-consistently calculated in order to reproduce the INMS composition.

[60] *Strobel* [2009] also concludes that high CH$_4$ escape fluxes are necessary to reproduce the INMS density and mixing ratio measurements. However, the author posits that this escape is driven from below due an upward propagation of energy, driven by solar heating and transported through thermal conduction. According to *Strobel* [2009], this mechanism is described as "slow, dense hydrodynamic escape," which produces the enhanced vertical speeds for CH$_4$. Like *Strobel* [2008, 2009], T-GITM employs the same collision-dominated form for thermal conduction. We also incorporate solar heating, and include HCN cooling self-consistently, but, unlike *Strobel* [2009], we cannot reproduce this hydrodynamic escape from the physics of the Navier-Stokes equations.

[61] T-GITM is a nonhydrostatic model, allowing for large upward flows and transonic solutions near intense, localized heating events [*Ridley et al.*, 2006]. Thus, if this enhanced escape is being driven from below by the physics contained within the Navier-Stokes equations, as suggested by *Strobel* [2009], then this escape should be present in the simulations by T-GITM. Instead, we find that this escape is not generated from below, but it must be imposed from above the modeling domain. Hence, based upon the results from models 1–3(NC), we conclude, as does *Tucker and Johnson* [2009], that, if large escape rates of CH$_4$ are

indeed occurring at Titan, then they must be driven by forces external to a 1-D Navier-Stokes model, such as (1) non-thermal plasma interactions with Titan's upper atmosphere or (2) global circulation of the planet that cannot be captured by a 1-D study.

[62] The escape speeds for H_2 in this study (between 90 and 100 m s^{-1}) are roughly a factor of 3 higher than those predicted by thermal Jeans escape alone (roughly 30–35 m s^{-1}). However, the mechanism responsible for such an enhancement of the escape speeds is currently poorly understood. *Cui et al.* [2008] suggests that 13-moment corrections to both the velocity distribution function (VDF) and the Navier-Stokes equations can account for this additional escape. T-GITM employs the same collision-dominated form for the stress tensor and heat flux vector as that utilized by *Cui et al.* [2008], yet it cannot reproduce this enhancement self-consistently. This discrepancy could be due to the fact that we use a single temperature, whereas *Cui et al.* [2008] allow separate N_2 and H_2 temperatures. However, *Strobel* [2009] indicates that this difference should be minor. Thus, we cannot currently account for the mechanism driving these enhanced H_2 vertical speeds. For the moment, we can only state that such speeds are required to reproduce the INMS H_2 densities of *Magee et al.* [2009].

4.4. Temperature and Density Structures Between 500 km and 1000 km

[63] Despite our best efforts at exactly replicating the conditions present in the works by *Cui et al.* [2008], *Strobel* [2009], and *Yelle et al.* [2008], there are notable differences between the thermal structure and densities below 1000 km employed in those works and the current study. The source for these major differences lies in how each study determines the thermal structure in Titan's upper atmosphere. In the work of *Cui et al.* [2008], *Strobel* [2009], and *Yelle et al.* [2008], there is no independent energy calculation.

[64] In the work of *Yelle et al.* [2008], the thermal structure is interpolated between 500 km and 1000 km. Above 1000 km, the temperatures are derived from N_2 density scale heights. Likewise, *Strobel* [2009, Figure 6] determines temperatures above and below 1000 km according to the nitrogen density scale heights. *Cui et al.* [2008] also infers temperatures below 1500 km according to the density scale heights of N_2. By contrast, T-GITM uses the Navier-Stokes equations to calculate temperatures that then determine the neutral density structures between 500 km to 1000 km.

[65] These differences in methodologies lead to significant discrepancies in the overall density structures between 500 km and 1000 km. In T-GITM, the total density at 500 km is set to 4.80×10^{19} m^{-3}, which is lower than either that of *Strobel* [2009] ($\sim 1.0 \times 10^{20}$) or that of *Yelle et al.* [2008] ($\sim 6.2 \times 10^{19}$). This can be directly attributed to the differences in the thermal structure between 500 km and 1000 km. In the work of *Strobel* [2009], the temperature at 500 km is set to $\sim$140 K, while *Yelle et al.* [2008] sets the temperature at 500 km to between 170 K and 180 K. In our simulations, we utilize a temperature of 160 K at 500 km that is consistent with low-latitude to midlatitude temperatures of *Achterberg et al.* [2008]. Ultimately, there appear to be many acceptable configurations for the densities and temperatures between 500 km and 1000 km.

[66] The uncertainties inherent in the CIRS and INMS measurements cannot provide strong constraints in this region. At 500 km, the CIRS measurements are subject to large uncertainties, since this altitude represents the upper limit of their measurement range [cf. *Achterberg et al.*, 2008]. In that work, the authors indicate that measurements less than 0.2 mbar are subject to a much higher degree of uncertainty. Moreover, the CIRS measurements are based upon pressure levels, which means that assigning an altitude to the measurements represents an additional source of uncertainty. This in turn, means that there are no strong observational constraints for modeling the atmosphere above 500 km. This conundrum is exemplified by the wide range of thermal and density structures used by *Strobel* [2009], *Yelle et al.* [2008], and the current work to reproduce the same INMS data set above 1000 km.

[67] Moreover, it appears that the thermal structure is not well determined above 1000 km, based solely upon INMS density measurements. Illustrating this point, Figures 2 and 3 show that there is no unique solution for the thermal structure that matches the density and mixing ratio measurements of INMS. In Figures 2 and 3, we depict three separate simulations that all equally explain the INMS measurements (see Table 4) with very different thermal structures. This suggests that, even when the density structures are relatively well constrained by INMS, these densities provide only a weak constraint for calculated temperatures in the upper atmosphere. Hence, despite our growing knowledge of Titan's upper atmosphere, significant uncertainties still exist above 500 km. Given these uncertainties, it appears that any estimates made about the thermal structure and escape rates of key species, such as CH_4, must also have concomitantly large uncertainties associated with them. In paper 2, we explore these uncertainties further, in order to find new configurations of Titan's upper atmosphere that do not rely upon large CH_4 escape rates to explain the INMS composition reported by *Magee et al.* [2009].

4.5. Importance of HCN

[68] Hydrogen Cyanide (HCN) represents the upper atmosphere's "thermostat," meaning that it is the key radiative species balancing solar, magnetospheric, and dynamical heating [*Yelle*, 1991; *Müller-Wodarg et al.*, 2000]. It serves as an analogue to CO_2 15-μ cooling in the atmospheres of Mars and Venus [cf. *Bougher et al.*, 1988; *Bougher and Dickinson*, 1988]. As shown in Figure 5, the longwave radiative cooling supplied by the HCN rotational lines greatly influences the energy budget at all altitudes between 500 and 1000 km, playing a critical role in determining the equilibrium temperature structure. This thermal structure then modifies the vertical dynamics and the chemical production and loss rates, through the temperature dependence of the chemical rate coefficients. Hence, self-consistently simulating HCN's chemical, dynamical, and energetic feedbacks remains crucial to our understanding of Titan's upper atmosphere.

[69] The various feedbacks between composition and energetics is illustrated in Figures 3a and 3d, depicting a wide range of simulated HCN mixing ratios and associated temperature profiles. Table 3 contains the total external heating rate imposed in each model. Upon inspection of Figure 3 and Table 3, notable trends emerge. First, those

simulations with the lowest HCN mixing ratios (models 3 and 3(NC)) do not require much external heating. These simulations, moreover, exhibit very small vertical gradients in their temperature structures at high altitudes. By contrast, the simulations with higher HCN mixing ratios require robust heating rates in order to match the INMS density measurements, which is shown by the contrast between model 1 (heating applied) and model 2 (no heating applied).

[70] The simulations with the lowest mixing HCN ratios (models 3 and 3(NC)) employ an artificially enforced maximum abundance at high altitudes. We choose this maximum value in order to be consistent with previous modeling work [i.e., *Strobel*, 2008; *Vuitton et al.*, 2006]. By contrast, the simulations possessing the higher mixing ratios of HCN (models 1 and 2) employ the HCN chemistry of Figure 1. The abundances of HCN predicted by models 1 and 2 compare favorably with recent work by *Krasnopolsky* [2009], which employs a much more detailed chemical scheme than that utilized here.

[71] In essence, we have shown two possible scenarios for HCN in our simulations: (1) an artificially imposed cap on HCN mixing ratios to limit the IR cooling or (2) a large amount of HCN with a simultaneously large exospheric heating rate to balance increased IR cooling. By limiting the HCN abundances at high altitudes, we are effectively increasing the homopause altitude for this species alone. It is well established that HCN and the homopause are intimately coupled [cf. *Wilson and Atreya*, 2004], whereby a higher homopause transports HCN downward more efficiently, reducing the amount of HCN high in the atmosphere. This suggests that the homopause altitude of 840 km is too low for HCN and that it should be raised in order to reduce the amount present in the upper atmosphere. In a later paper, we focus on the composition analysis by *Magee et al.* [2009], whose independent ^{40}Ar abundances support a higher homopause and reduce the abundances of HCN. If, on the other hand, one adheres to the lower homopause altitude of 840 km, then one must then either (1) impose robust external heating rates or (2) posit additional physicochemical loss process for HCN (such as aerosol trapping/adsorption) as in the work of *Liang et al.* [2007].

[72] Next, we address the nature of this external heating rate that we must impose at 1500 km for model 1. The range of external heating rates utilized in this study (between 0.0 and 150.0 eV cm^{-3} s^{-1}) remains consistent with recent modeling efforts [*De La Haye et al.*, 2007a, 2007b; *Johnson et al.*, 2009]. These studies find that plasma heating is occurring in the upper atmosphere and is highly variable, ranging from 0.0 to 250.0 eV cm^{-3} s^{-1} with a mean value of ~100 eV cm^{-3} s^{-1}, based upon analysis of Cassini data [*Johnson et al.*, 2009]. Most likely, this heat influx is due to a combination of processes that are not accounted for in the 1-D version of T-GITM, such as (1) Joule heating and/or ion drag, (2) energetic particle precipitation, (3) the general circulation of the planet, and (4) heating by upward propagating gravity waves [*Strobel*, 2006]. However, there are important limitations to the T-GITM results and our conclusions, due to the boundary conditions imposed on HCN at 500 km.

[73] Setting a fixed mixing ratio at 500 km for HCN artificially modifies this species' abundances below 700 km. Above 700 km, we find that the HCN profile is insensitive to the lower boundary. If we instead allow the model to calculate the mixing ratios of HCN at 500 km without constraints, then the abundances at 500 km can deviate markedly from the values established by CIRS at 500 km by *Teanby et al.* [2007]. This occurs principally because the chemistry of Figure 1 captures only the major chemical production and loss mechanisms for HCN above 500 km. This scheme cannot account for the important chemistry below 500 km identified by *Krasnopolsky* [2009]. Also, recent analysis of stratospheric CIRS data suggests that HCN may interact strongly with the ambient aerosol population, resulting in a net loss of HCN to the aerosols and explaining the sharp gradients in the CIRS-derived abundance profiles in the stratosphere [cf. *Vinatier et al.*, 2007; *Teanby et al.*, 2008].

[74] Given the large amount of chemistry and heterogenous processes likely occurring below 500 km, T-GITM cannot self-consistently calculate fluxes for HCN at the lower boundary, which is why we opt to fix the abundances using the CIRS mixing ratio measurements of *Teanby et al.* [2007]. Effectively, instead of attempting to artificially constrain fluxes so that the mixing ratios match CIRS observations at 500 km, we have specified those measurements in the model. Because this method is not truly a self-consistent treatment, it represents a potential limitation of the present study and its conclusions. Ultimately, the complex chemistry of Titan's atmosphere precludes us from a truly self-consistent treatment of this key radiative molecule, but we have attempted to constrain it using the most relevant measurements from CIRS at 500 km and INMS above 1000 km.

5. Conclusions

[75] We have presented a series of calibration simulations for the newly developed Titan Global Ionosphere-Thermosphere Model. Models 1, 3, and 3(NC) have demonstrated that the T-GITM framework can successfully reproduce the INMS density and mixing ratios measurements of *Magee et al.* [2009] to within ~10%, validating the model's capabilities. Furthermore, from these simulations, we have arrived at the following main conclusions:

[76] 1. Using the ^{40}Ar mixing ratios of *Yelle et al.* [2008], a homopause altitude of roughly 840 km is imposed on methane and enhanced escape fluxes of CH$_4$, ranging from 1.64 to 2.64 × 10^{13} molecules m^{-2} s^{-1}, are required in order to reproduce the INMS composition measurements. These escape rates are consistent with the work by *Strobel* [2009] and *Yelle et al.* [2008], using similar parameters.

[77] 2. These enhanced escape rates of methane must be imposed upon the modeling domain and cannot be self-consistently calculated by T-GITM. This suggests that the CH$_4$ escape, if present, is driven by external mechanisms, such as global transport or nonthermal processes as suggested by *Tucker and Johnson* [2009].

[78] 3. H$_2$ attains nearly its limiting flux with topside escape fluxes ranging between 1.02 and 1.06 × 10^{14} molecules m^{-2} s^{-1} consistent with *Cui et al.* [2008] and *Strobel* [2009]. The escape speeds (~90 m s^{-1}) required for H$_2$ must be imposed upon T-GITM, and the model cannot self-consistently account for the enhancement over Jeans escape.

[79] 4. Large uncertainties in the temperatures and densities between 500 km and 1000 km allow for a large range

of potential configurations of Titan's upper atmosphere. Above 1000 km, where INMS has provided improved constraints on densities and mixing ratios, there are many possible thermal structures that can reproduce the INMS measurements equally well. This is clearly shown by the different temperature profiles in models 1, 3, and 3(NC).

[80] 5. We find that including HCN chemistry and subsequent IR cooling in the model is critical to self-consistently simulating the upper atmosphere. However, boundary conditions on HCN mixing ratios at 500 km are difficult to impose, due to the large amount of chemical reactions occurring below 500 km and the complex interactions between HCN and ambient aerosols.

Appendix A: Detailed Fluid Equations

A1.   T-GITM Numerics

[81] In the following section, we delineate the radial equations solved by the Titan model and defer discussion of the full 3-D model to future publications. Furthermore, we focus on the neutral dynamics and thermal structure calculations. For a complete development of the numerical methods, we refer readers to *Ridley et al.* [2006]. In the radial direction, each species possesses an unique velocity. These velocities are coupled through bimolecular friction forces taken after *Colegrove et al.* [1966]. The radial set of fluid equations compensate for the exponential nature of the atmosphere by numerically solving for the logarithm of densities, rather than the neutral densities themselves. We define the natural logarithm of the neutral densities, $\mathcal{N}_s$, as follows:

$$\mathcal{N}_s = \ln(n_s), \tag{A1}$$

where n_s is the neutral density of species "s" in (m^{-3}).

A1.1.   Radial Continuity

[82] In rotating spherical coordinates, the vertical continuity equation can be written as follows:

$$\frac{\partial \mathcal{N}_s}{\partial t} + \frac{\partial u_{r,s}}{\partial r} + \frac{2u_{r,s}}{r} + u_{r,s}\frac{\partial \mathcal{N}_s}{\partial r} = \frac{1}{n_s}C_s, \tag{A2}$$

where $u_{r,s}$ is the species' velocity $(m\ s^{-1})$ in the radial direction, and C_s is the species-specific chemical source function given by

$$C_s = P_s - L_s, \tag{A3}$$

where P_s is the chemical source term and L_s the chemical loss term $(m^{-3}\ s^{-1})$.

A1.2.   Radial Momentum

[83] In rotating spherical polar coordinates, the individual species' momentum equations are given as

$$\frac{\partial u_{r,s}}{\partial t} + u_{r,s}\frac{\partial u_{r,s}}{\partial r} + \frac{u_\theta}{r}\frac{\partial u_{r,s}}{\partial \theta} + \frac{u_\phi}{r\cos\theta}\frac{\partial u_{r,s}}{\partial \phi} + \frac{k}{m_s}\frac{\partial T}{\partial r} + T\frac{k}{m_s}\frac{\partial \mathcal{N}_s}{\partial r}$$
$$= g + \mathcal{F}_s + \frac{F^{turb}}{\rho} + \frac{u_\theta^2 + u_\phi^2}{r} + r\Omega^2\cos^2\theta + 2\Omega u_\phi\cos\theta, \tag{A4}$$

where θ is north latitude, ϕ is east longitude, u_θ and u_ϕ are the northward and eastward components of the mean neutral

velocity $(m\ s^{-1})$. Ω is the planetary rotation rate (s^{-1}), g is the gravitational acceleration $(m\ s^{-2})$. The term, $\mathcal{F}_s$, contains the neutral-neutral momentum coupling term of *Colegrove et al.* [1966], *Schunk and Nagy* [2000], and *Gombosi* [1999]:

$$\mathcal{F}_s = \frac{kT}{m_s}\frac{1}{N}\sum_{q\neq s}\frac{n_q}{D_{sq}}\left(u_{r,q} - u_{r,s}\right). \tag{A5}$$

In this equation, D_{sq} represents the binary molecular diffusion coefficient $(m^2\ s^{-1})$ between neutral species s and q, as formulated by *Banks and Kockarts* [1973].

[84] Including the effects of turbulence directly into the momentum equation represents a break from previous formulations. An explicit mixing force, $\frac{F^{turb}}{\rho}$, parameterizes the effects of unresolved atmospheric turbulence by constraining minor constituents to follow the mean atmosphere scale height.

$$\frac{F^{turb}}{\rho_s} = \frac{kT}{m_s}\frac{1}{N}\sum_{q\neq s}\frac{n_q}{D_{sq}}\left[\omega_s^E - \omega_q^E\right]. \tag{A6}$$

[85] In this last expression we define ω_s^E as

$$\omega_s^E = -K(r)\frac{1}{\chi_s}\frac{\partial \chi_s}{\partial r}. \tag{A7}$$

A more complete discussion of turbulence and its implementation in the Titan model occurs in Appendix B.

A1.3.   Radial Energy

[86] The T-GITM radial energy equation is given by

$$\frac{\partial T}{\partial t} + u_r\frac{\partial T}{\partial r} + (\gamma - 1)T\left(2\frac{u_r}{r} + \frac{\partial u_r}{\partial r}\right) + \frac{1}{\rho c_v}\eta\left(\frac{\partial u_r}{\partial r}\right)^2 = \frac{Q_{tot}}{\rho c_v}, \tag{A8}$$

$$Q_{tot} = Q_{EUV} - Q_{HCN} + Q_{external} + \frac{1}{r^2}\frac{\partial}{\partial r}\left[r^2\kappa_m\frac{\partial T}{\partial r}\right]. \tag{A9}$$

Here, Q_{tot} is the total exogenous source function, which is composed of solar EUV forcing (Q_{EUV}), HCN rotational line cooling (Q_{HCN}), External heating $(Q_{external})$. The final term on the right hand side of equation (A9) represents molecular thermal conduction. $\gamma = \frac{c_p}{c_v}$ is the ratio of specific heats and η is the molecular viscosity coefficient. The coefficient κ_m represents the molecular conductivity $(W\ (m\ K)^{-1})$.

A1.4.   External Heating Calculations in This Work

[87] For the purposes of this work, the details of the external heating remain unimportant. Instead, we concern ourselves only with the amount of heating at the top of the atmosphere. By external heating, we are including all possible heating sources that are not explicitly incorporated in the 1-D T-GITM framework. This can include, for example, horizontal transport from other regions of the atmosphere.

[88] However, without further information, we abstract all additional energy inputs into this external heating rate and we assume that this energy flux is deposited in the top layers of T-GITM. This external heating should be taken as an

upper limit on net energy input into the upper atmosphere. For reference, we assume the following relationship:

$$-\nabla \cdot \mathbf{F} = Q_{external}. \tag{A10}$$

[89] In this equation, $\mathbf{F}$ is the incident heat flux (in W m^{-2}) and $Q_{external}$ is the volumetric heating rate (W m^{-3}). For the purposes of this work, we assume that the Flux is completely deposited in this top layer. Thus, dropping the terms proportional to $\frac{1}{r}$, we have the following very simplified expression:

$$\frac{d\mathbf{F}}{dr} = -Q_{external}. \tag{A11}$$

[90] A $Q_{external}$ on the order of 100 eV cm^{-3} s^{-1} corresponds, within the context of the GITM computational model, to an incident flux of energy equivalent to 2.0×10^8 eV cm^{-2} $^{-1}$s, which is consistent with the magnitudes of plasma heating considered by *Strobel* [2009].

A2. Viscosity, Thermal Conductivity, and Molecular Diffusion Coefficients

[91] In this section, we provide details for the physical parameters used in the Navier-Stokes equations of the previous section.

A2.1. Specific Heat at a Constant Volume

[92] A number density–weighted mean of the N_2 and CH_4 specific heats is employed, as follows:

$$c_v = \left(\frac{n_{N_2}}{N}\right) c_{v,N_2} + \left(\frac{n_{CH_4}}{N}\right) c_{v,CH_4}. \tag{A12}$$

Here, T-GITM adopts the values of $c_{v,N_2} = \frac{5}{2}\frac{k}{m_{N_2}}$ and $c_{v,CH_4} = \frac{6.5374}{2}\frac{k}{m_{CH_4}}$ (J (kg K)$^{-1}$) [*Serway*, 1996].

A2.2. Viscosity

[93] T-GITM calculates the dynamic viscosity coefficient, η, from a mass-weighted mean of the N_2 and CH_4 viscosities:

$$\eta = \left(\frac{\rho_{N_2}}{\rho}\right)\eta_{N_2} + \left(\frac{\rho_{CH_4}}{\rho}\right)\eta_{CH_4}. \tag{A13}$$

In order to calculate η_{N_2}, the model employs the Sutherland formula for η_{N_2} [*De La Haye*, 2005; *Crane Company*, 1988; *Weast*, 1984], which is given by

$$\eta_{N_2} = \eta_{0,N_2}\frac{T_{0,N_2} + C_{N_2}}{T + C_{N_2}}\left(\frac{T}{T_{0,N_2}}\right)^{\frac{3}{2}}. \tag{A14}$$

Here, $T_{0,N_2} = 300.55$ K and $\eta_{0,N_2} = 0.01781$ centipoise [*Weast*, 1984], are the reference temperature and associated viscosity for Nitrogen. $C_{N_2} = 111$ K is the Sutherland constant for nitrogen [*Crane Company*, 1988]. For methane, the model adopts the empirical expression from *Yaws* [1995], valid between 95 and 850 K, and is given by (in centipoise)

$$\eta_{CH_4} = \left(3.8435 + 4.0112 \times 10^{-1}T - 1.4303 \times 10^{-4}T^2\right) \times 10^{-4}. \tag{A15}$$

A2.3. Thermal Conductivity

[94] The molecular conductivity used in T-GITM represents a combination of both N_2 and CH_4 molecular conductivities. For N_2, the model utilizes the formulation of *Yaws* [1997, 1995]:

$$\kappa_{N_2}(T) = 0.00309 + 7.593 \times 10^{-5}T - 1.1014 \times 10^{-8}T^2$$
$$78K \leq T \leq 1500K, \tag{A16}$$

$$\kappa_{CH_4}(T) = -0.00935 + 1.4028 \times 10^{-4}T + 3.318 \times 10^{-8}T^2$$
$$97K \leq T \leq 1400K. \tag{A17}$$

Because CH_4 is nonnegligible in Titan's upper atmosphere, T-GITM must employ a mixture conductivity, which for polyatomic gases is given by *Mason and Saxena* [1958]:

$$\kappa_{mix} = \sum_i \kappa_i \left(1 + \sum_{j\neq i} G_{ij}\frac{x_i}{x_j}\right)^{-1}, \tag{A18}$$

where x_i is the mole fraction of the ith species and where G_{ij} is given by

$$G_{ij} = \frac{1.065}{2\sqrt{2}}\left(1 + \frac{m_i}{m_j}\right)^{-\frac{1}{2}}\left[1 + \left(\frac{\kappa_i^0}{\kappa_j^0}\right)^{\frac{1}{2}}\left(\frac{m_i}{m_j}\right)^{\frac{1}{4}}\right]^2. \tag{A19}$$

Here, κ_i is the ith species' individual thermal conductivity and κ_i^0 represents the frozen thermal conductivity of species. The ratio of the κ_i^0's can be expressed as in the work of *Mason and Saxena* [1958]:

$$\frac{\kappa_i^0}{\kappa_j^0} = \frac{\eta_i m_j}{\eta_j m_i}. \tag{A20}$$

A2.4. Molecular Diffusion Coefficients

[95] D_{sq} represents the binary molecular diffusion coefficient between neutral species q and s, as formulated by *Banks and Kockarts* [1973]:

$$D_{sq} = \frac{A_{sq}T^b}{N}. \tag{A21}$$

In T-GITM, the values for the most significant A_{sq} coefficients are given in Table A1. A number of the necessary values for these binary diffusion coefficients are available in the literature [cf. *Banks and Kockarts*, 1973; *Mason and Marrero*, 1970; *Massman*, 1998] for the species included in the Titan GITM model. However, where binary diffusion coefficients could not be obtained directly, we employ the analytical approximation given by *De La Haye* [2005] and *Wilson and Atreya* [2004]:

$$if\ m_s > m_q \rightarrow D_{sq} = D_{ss}\sqrt{\frac{1/m_s + 1/m_q}{2/m_s}}, \tag{A22}$$

$$if\ m_s \leq m_q \rightarrow D_{sq} = D_{ss}\sqrt{\frac{m_s}{m_q}}. \tag{A23}$$

Table A1. Selected Binary Diffusion Coefficients, $D_{qs} = \frac{A_{qs}T^b}{N}$ in cm^2 s^{-1}

Interacting Species	$A_{q,s}$	b	Reference
$N_2 - N_2$	5.09×10^{16}	0.810	*Massman* [1998]
$CH_4 - CH_4$	5.73×10^{16}	0.765	*Wilson* [2002], *Reid et al.* [1987]
$N_2 - CH_4$	7.34×10^{16}	0.750	*Massman* [1998]
$N_2 - H_2$	1.88×10^{17}	0.820	*Banks and Kockarts* [1973]
$CH_4 - H_2$	2.30×10^{17}	0.765	*Mason and Marrero* [1970]

A2.5. Running T-GITM

[96] The Titan Global Ionosphere-Thermosphere Model, in its full 3-D mode, runs with a uniform horizontal resolution of 2.5° in latitude and 5° in longitude, since the variations of key prognostic variables ($\mathbf{u}$, T, and n) are found to be much greater in latitude than in longitude [*Müller-Wodarg et al.*, 2006, 2008]. However, the GITM framework remains very flexible and can accommodate any desired resolution in latitude, longitude, and altitude. In the radial direction, T-GITM spans the altitude range from 500 km to 1500 km and possesses a nonuniform grid. The resolution at 500 km is 2.5 km and the grid spacing rises to a uniform 10.0 km above 600 km.

[97] T-GITM remains an explicit time stepping model, resulting in very small time steps that are limited to roughly 1 second. For specific examples of T-GITM's runtime, we provide two cases. First, the 1-D model can run an entire Earth year in 12 h of wall clock time on the Lonestar Linux Cluser, which is part of the Texas Advanced Computing Center (TACC). In a full 3-D model with 2.5° in latitude and 5° in longitude resolution, we find that T-GITM runs 8.5 Earth days in 8 h of wall clock time on 288 processors.

Appendix B: Details of the Turbulence Formulation in T-GITM

[98] Titan GITM parameterizes the impacts of subgrid-scale turbulence on the mixing of key minor constituents through a heuristic eddy diffusion coefficient, denoted K(r) [*Atreya*, 1986]. In the canonical derivation, the impacts of this turbulence are introduced into the momentum equation after several approximations are made, as in the work of *Colegrove et al.* [1966], *Schunk and Nagy* [2000], and *Gombosi* [1999]. However, it has become common practice in other Global Circulation Models (GCMs) to include the impacts of this turbulence in the continuity equation [*Roble et al.*, 1988; *Fuller-Rowell and Rees*, 1980, 1983; *Müller-Wodarg et al.*, 2000]. Most recently, *Boqueho and Blelly* [2005] developed a 13-moment model that possesses a vertical momentum equation similar to that of T-GITM and they have incorporated turbulence into the momentum equation. Likewise, we have also incorporated turbulence directly into the vertical momentum equation.

[99] According to *Colegrove et al.* [1966], *Schunk and Nagy* [2000], and *Gombosi* [1999], the radial momentum equation of the Navier-Stokes equations (without turbulence and omitting ion-neutral coupling) is given by

$$\frac{\partial \mathbf{u_s}}{\partial t} + \mathbf{u_s} \cdot \nabla \mathbf{u_s} + \frac{\nabla p_s}{\rho_s} - \mathbf{g} + \frac{\nabla \cdot \tau_s}{\rho_s} + \mathbf{a}_s = \left(\frac{\delta \mathbf{u_s}}{\delta t}\right)^{neutral-neutral}.$$

(B1)

In the above expression, $\left(\frac{\delta \mathbf{u_s}}{\delta t}\right)^{neutral-neutral}$ represents the contribution due to neutral-neutral frictional drag, $\frac{\Delta \cdot \tau_s}{\rho_s}$ represents the viscosity shear forces, $\mathbf{a}_s$ represents accelerations due to Coriolis and curvature forces, and finally $\mathbf{g}$ represents the gravitational acceleration. Mathematically, the neutral-neutral frictional term is given by *Colegrove et al.* [1966] as

$$\left(\frac{\delta \mathbf{u}}{\delta t}\right)^{neutral-neutral} = \frac{kT}{m_s}\frac{1}{N}\sum_{q\neq s}\frac{n_q}{D_{sq}}\left(\mathbf{u}_q - \mathbf{u}_s\right).$$

(B2)

In this expression, all symbols have their usual definitions from previous sections. Next, turbulence is added to the right-hand side of the momentum equation, according to *Colegrove et al.* [1966] in the following form:

$$\left(\frac{\delta \mathbf{u}}{\delta t}\right)^{turbulent} = \frac{kT}{m_s}\frac{1}{N}\sum_{q\neq s}\frac{n_q}{D_{sq}}\omega_s^E.$$

(B3)

[100] In this last expression, ω_s^E represents the turbulent velocity for species "s." Finally, one arrives at a formulation for the Navier-Stokes momentum equation that includes turbulence as follows (while still ignoring the ion-neutral coupling):

$$\frac{\partial \mathbf{u_s}}{\partial t} + \mathbf{u_s} \cdot \nabla \mathbf{u_s} + \frac{\nabla p_s}{\rho_s} - \mathbf{g} + \frac{\nabla \cdot \tau_s}{\rho_s} + \mathbf{a}_s$$
$$= \frac{kT}{m_s}\frac{1}{N}\sum_{q\neq s}\frac{n_q}{D_{sq}}\left(\mathbf{u}_q - \mathbf{u}_s\right) + \frac{kT}{m_s}\frac{1}{N}\sum_{q\neq s}\frac{n_q}{D_{sq}}\omega_s^E.$$

(B4)

[101] This formulation represents a significant break from previous Global modeling frameworks. In particular, treating both molecular and turbulent diffusion in the momentum equation represents a novel approach, pioneered by the work of *Boqueho and Blelly* [2005] in a 1-D 13-moment model for Mars' upper atmosphere. Given this new formulation, it remains prudent to consider whether or not this method will conserve momentum when summed over all species.

[102] First, one begins with equation (B4) and takes the following approximations: (1) Assume a near steady state, such that $\frac{\partial \mathbf{u_s}}{\partial t} = 0.0$. (2) Assume that, in a near steady state, one may drop the terms $\mathbf{u_s} \cdot \nabla \mathbf{u_s}$ and $\frac{\nabla \cdot \tau_s}{\rho_s}$. (3) Finally, let $g_{eff} = g - a_s$, which represents the effective gravitational force. The resulting reduced momentum equation, after multiplying both sides by ρ_s, emerges as [cf. *Schunk and Nagy*, 2000; *Gombosi*, 1999]

$$\nabla p_s - \rho_s \mathbf{g}_{eff} = \rho_s\left(\frac{kT}{m_s}\frac{1}{N}\sum_{q\neq s}\frac{n_q}{D_{sq}}\left(\mathbf{u}_q - \mathbf{u}_s\right) + \frac{kT}{m_s}\frac{1}{N}\sum_{q\neq s}\frac{n_q}{D_{sq}}\omega_s^E\right).$$

(B5)

[103] Now, if we sum equation (B5) over all species, then we arrive at the following:

$$\sum_s (\nabla p_s - \rho_s \mathbf{g}_{eff}) = \sum_s \left[\rho_s\left(\frac{kT}{m_s}\frac{1}{N}\sum_{q\neq s}\frac{n_q}{D_{sq}}\left(\mathbf{u}_q - \mathbf{u}_s\right)\right.\right.$$
$$\left.\left. + \frac{kT}{m_s}\frac{1}{N}\sum_{q\neq s}\frac{n_q}{D_{sq}}\omega_s^E\right)\right].$$

(B6)

On the right-hand side of equation (B6), the neutral-neutral coupling term identically sums to zero, because, by definition the Molecular diffusion coefficients are symmetric with respect to index change, $D_{sq} = D_{qs}$. This causes equation (B6) to reduce to the following:

$$\nabla p - \rho \mathbf{g_{eff}} = \sum_s \left[\rho_s \frac{kT}{m_s} \frac{1}{N} \sum_{q \neq s} \frac{n_q}{D_{sq}} \omega_s^E \right], \qquad (B7)$$

where we have introduced the total pressure, $p = \sum_s p_s$ and the total mass density $\rho = \sum_s \rho_s$. In order to have a stable atmosphere, we demand that the total atmosphere be in roughly a hydrostatic equilibrium. In other words, in a steady state and absent any significant external driving forces, we demand that the bulk atmosphere satisfy the following relationship:

$$\nabla p - \rho \mathbf{g_{eff}} = 0.0. \qquad (B8)$$

However, this condition remains equivalent to demanding that the following holds identically:

$$\sum_s \left[\rho_s \frac{kT}{m_s} \frac{1}{N} \sum_{q \neq s} \frac{n_q}{D_{sq}} \omega_s^E \right] = 0.0. \qquad (B9)$$

Unfortunately, there seems to be no way of guaranteeing this condition a priori without first choosing a proper form for the eddy velocities, ω_s^E. In order to guarantee that equation (B8) holds regardless of one's choice for ω_s^E, we introduce a variation on the turbulent force as follows:

$$\left(\frac{\delta \mathbf{u}}{\delta t} \right)^{turbulent} = \frac{kT}{m_s} \frac{1}{N} \sum_{q \neq s} \frac{n_q}{D_{sq}} \left(\omega_s^E - \omega_q^E \right). \qquad (B10)$$

This new turbulent force appears completely analogous to the neutral-neutral coupling term. With this form of the turbulent contribution to the velocities, equation (B7) now becomes

$$\nabla p - \rho \mathbf{g_{eff}} = \sum_s \left[\rho_s \frac{kT}{m_s} \frac{1}{N} \sum_{q \neq s} \frac{n_q}{D_{sq}} \left(\omega_s^E - \omega_q^E \right) \right]. \qquad (B11)$$

Again, because of the symmetry properties of the coefficients, D_{sq}, we now have that equation (B8) holds for the total atmosphere in a steady state. Thus, we adopt the turbulent contribution given by equation (B10) in the T-GITM framework.

[104] Next, one must choose the functional form for the eddy velocities, ω_s. In the literature, the most common turbulent velocity formulation occurs as [*Colegrove et al.*, 1966; *Schunk and Nagy*, 2000; *Gombosi*, 1999]

$$\omega_s^E = -K(r) \frac{1}{\chi_s} \frac{\partial \chi_s}{\partial r}, \qquad (B12)$$

where χ_s is the volume mixing ratio, defined as $\chi_s = \frac{n_s}{\sum_s n_s}$. Thus, the full momentum equation employed in this work emerges as follows:

$$\frac{\partial \mathbf{u_s}}{\partial t} + \mathbf{u_s} \cdot \nabla \mathbf{u_s} + \frac{\nabla p_s}{\rho_s} - \mathbf{g} + \frac{\nabla \cdot \tau_s}{\rho_s} + \mathbf{a_s} = \frac{kT}{m_s} \frac{1}{N} \sum_{q \neq s} \frac{n_q}{D_{sq}} \left(\mathbf{u_q} - \mathbf{u_s} \right)$$
$$- \frac{kT}{m_s} \frac{1}{N} \sum_{q \neq s} \frac{n_q K(r)}{D_{sq}} \left[\frac{1}{\chi_s} \frac{\partial \chi_s}{\partial r} - \frac{1}{\chi_q} \frac{\partial \chi_q}{\partial r} \right]. \qquad (B13)$$

[105] This new formulation has the virtue of being continuous, applicable, and stable throughout all regions of the atmosphere. Thus, while we use the previous works by *Colegrove et al.* [1966] and *Boqueho and Blelly* [2005] as inspiration, the method of turbulence used here remains unique to GITM and this represents its first instance in publication.

References

Achterberg, R. K., B. J. Conrath, P. J. Gierasch, F. M. Flasar, and C. A. Nixon (2008), Titan's middle-atmospheric temperatures and dynamics observed by the Cassini Composite Infrared Spectrometer, *Icarus*, *194*, 263–277.

Atreya, S. K. (1986), *Atmospheres and Ionospheres of the Outer Planets and Their Satellites*, Phys. Chem. Space Ser., vol. 15, Springer, New York.

Banks, P. M., and G. Kockarts (1973), *Aeronomy*, 3rd ed., Academic Press, New York.

Bell, J. M., J. H. Waite, B. A. Magee, K. E. Mandt, and J. Westlake (2009), Simulating the 3-D structure of Titan's upper atmosphere, *Eos Trans. AGU*, *90*(22), Jt. Assem. Suppl., Abstract P11A-04.

Boqueho, V., and P.-L. Blelly (2005), Contributions of a multimoment multispecies approach in modeling planetary atmospheres: Example of Mars, *J. Geophys. Res.*, *110*, A01313, doi:10.1029/2004JA010414.

Bougher, S. W., and R. E. Dickinson (1988), Mars mesosphere and thermosphere: 1. Global mean heat budget and thermal structure, *J. Geophys. Res.*, *93*, 7325–7337.

Bougher, S. W., R. G. E. Roble, R. E. Dickinson, and E. C. Ridley (1988), Venus mesosphere and thermosphere. III - Three-dimensional general circulation with coupled dynamics and composition, *Icarus*, *73*, 545–573.

Boughner, R. E. (1985), Comparison of band model calculations of upper atmospheric cooling rates for the 15-micrometer carbon dioxide band, *J. Geophys. Res.*, *90*, 8011–8018.

Chandrasekhar, S. (1960), *Radiative Transfer*, Dover, New York.

Clarke, D. W., and J. P. Ferris (1997), Chemical evolution on Titan: Comparisons to the prebiotic Earth, *Origins Life Evol. Biospheres*, *27*, 225–248.

Colegrove, F. D., F. S. Johnson, and W. B. Hanson (1966), Atmospheric composition in the lower thermosphere, *J. Geophys. Res.*, *71*, 2227–2236.

Crane Company (1988), Flow of fluids through valves, fittings, and pipes, *Tech. Pap.*, *410*, Chicago, Ill.

Crary, F. J., B. A. Magee, K. Mandt, J. H. Waite, J. Westlake, and D. T. Young (2009), Heavy ions, temperatures and winds in Titan's ionosphere: Combined Cassini CAPS and INMS observations, *Planet. Space Sci.*, *57*, 1847–1856.

Cravens, T. E., et al. (2009), Model-data comparisons for Titan's nightside ionosphere, *Icarus*, *199*, 174–188.

Cui, J., R. V. Yelle, and K. Volk (2008), Distribution and escape of molecular hydrogen in Titan's thermosphere and exosphere, *J. Geophys. Res.*, *113*, E10004, doi:10.1029/2007JE003032.

Cui, J., et al. (2009), Analysis of Titan's neutral upper atmosphere from Cassini Ion-Neutral Mass Spectrometer measurements, *Icarus*, *200*, 581–615.

De La Haye, V. (2005), Coronal formation and heating efficiencies in Titan's upper atmosphere: Construction of a coupled ion, neutral and thermal

structure model to interpret the first INMS Cassini data, Ph.D. thesis, Univ. of Mich., Ann Arbor.

De La Haye, V., J. H. Waite, T. E. Cravens, A. F. Nagy, R. E. Johnson, S. Lebonnois, and I. P. Robertson (2007a), Titan's corona: The contribution of exothermic chemistry, *Icarus*, *191*, 236–250.

De La Haye, V., et al. (2007b), Cassini Ion and Neutral Mass Spectrometer data in Titan's upper atmosphere and exosphere: Observation of a suprathermal corona, *J. Geophys. Res.*, *112*, A07309, doi:10.1029/2006JA012222.

De La Haye, V., J. H. Waite, T. E. Cravens, S. W. Bougher, I. P. Robertson, and J. M. Bell (2008a), Heating Titan's upper atmosphere, *J. Geophys. Res.*, *113*, A11314, doi:10.1029/2008JA013078.

De La Haye, V., J. H. Waite, T. E. Cravens, I. P. Robertson, and S. Lebonnois (2008b), Coupled ion and neutral rotating model of Titan's upper atmosphere, *Icarus*, *197*, 110–136.

Deng, Y., and A. J. Ridley (2007), Possible reasons for underestimating Joule heating in global models: E field variability, spatial resolution, and vertical velocity, *J. Geophys. Res.*, *112*, A09308, doi:10.1029/2006JA012006.

Deng, Y., A. D. Richmond, A. J. Ridley, and H.-L. Liu (2008), Assessment of the non-hydrostatic effect on the upper atmosphere using a general circulation model (GCM), *Geophys. Res. Lett.*, *35*, L01104, doi:10.1029/2007GL032182.

Fels, S. B., and M. D. Schwarzkopf (1981), An efficient, accurate algorithm for calculating CO_2 15 μm band cooling rates, *J. Geophys. Res.*, *86*, 1205–1232.

Flasar, F. M., et al. (2005), Titan's atmospheric temperatures, winds, and composition, *Science*, *308*, 975–978.

Fuller-Rowell, T. J., and D. Rees (1980), A three-dimensional time-dependent global model of the thermosphere, *J. Atmos. Sci.*, *37*, 2545–2567.

Fuller-Rowell, T. J., and D. Rees (1983), Derivation of a conservation equation for mean molecular weight for a two-constituent gas within a three-dimensional, time-dependent model of the thermosphere, *Planet. Space Sci.*, *31*, 1209–1222.

Gombosi, T. I. (1999), *Physics of the Space Environment*, Cambridge Univ. Press, New York.

Goody, R. M., and Y. L. Yung (1989), *Atmospheric Radiation: Theoretical Basis*, 2nd ed., Oxford Univ. Press, New York.

Hinteregger, H. E., K. Fukui, and B. R. Gilson (1981), Observational, reference and model data on solar EUV, from measurements on AE-E, *Geophys. Res. Lett.*, *8*, 1147–1150.

Houghton, J. T. (2002), *The Physics of Atmospheres*, 3rd ed., 320 pp., Cambridge Univ. Press, Cambridge, U. K.

Humlícek, J. (1982), Optimized computation of the Voigt and complex probability functions, *J. Quant. Spectrosc. Radiat. Transfer*, *27*, 437–444.

Hunten, D. M. (1973), The escape of H_2 from Titan, *J. Atmos. Sci.*, *30*, 726–732.

Hunten, D. M. (1974), Energetics of thermospheric eddy transport, *J. Geophys. Res.*, *79*, 2533–2534.

Johnson, R. E., O. J. Tucker, M. Michael, E. C. Sittler, D. T. Young, and J. H. Waite (2009), Mass loss processes in Titan's upper atmosphere, in *Titan From Cassini-Huygens*, edited by R. Brown, pp. 373–390, Springer, New York.

Krasnopolsky, V. A. (2009), A photochemical model of Titan's atmosphere and ionosphere, *Icarus*, *201*, 226–256.

Kuntz, M. (1997), A new implementation of the Humlicek algorithm for the calculation of the Voigt profile function, *J. Quant. Spectrosc. Radiat. Transfer*, *57*, 819–824.

Lebonnois, S. É., E. L. O. Bakes, and C. P. McKay (2003), Atomic and molecular hydrogen budget in Titan's atmosphere, *Icarus*, *161*, 474–485.

Lether, F. G., and P. R. Wenston (1991), The numerical computation of the Voigt function by a correlated midpoint quadrature rule for $(-\infty, \infty)$, *J. Comput. Appl. Math.*, *34*, 75–92.

Liang, M.-C., A. N. Heays, B. R. Lewis, S. T. Gibson, and Y. L. Yung (2007), Source of nitrogen isotope anomaly in HCN in the atmosphere of Titan, *Astrophys. J.*, *664*, L115–L118.

Lindfield, G. R., and J. Penny (1999), *Numerical Methods Using Matlab*, 2nd ed., Prentice Hall, Upper Saddle River, N. J.

Magee, B., J. H. Waite, K. Mandt, J. Westlake, J. M. Bell, and D. A. Gell (2009), INMS derived composition of Titan's upper atmosphere: Analysis methods and model comparisons, *Planet. Space Sci.*, *57*, 1895–1916.

Mandt, K. E., J. H. Waite, W. Lewis, B. A. Mageel, J. M. Bell, J. Luninel, O. Mousis, and D. Cordier (2009), Isotopic evolution of the major constituents of Titan's atmosphere based on Cassini data, *Planet. Space Sci.*, *57*, 1917–1930.

Martin, P. G., C. Rogers, and G. B. Rybicki (1984), Half-range moment methods for radiative transfer in spherical geometry. II - Implementation of the method, *Astrophys. J.*, *284*, 317–326.

Mason, E. A., and T. R. Marrero (1970), The diffusion of atoms and molecules, *Adv. At. Mol. Phys.*, *6*, 155–232.

Mason, E. A., and S. C. Saxena (1958), Approximate formula for the thermal conductivity of gas mixtures, *Phys. Fluids*, *1*, 361–369.

Massman, W. J. (1998), A review of the molecular diffusivities of H_2O, CO_2, CH_4, CO, O_3, SO_2, NH_3, N_2O, NO, and NO_2 near STP, *Atmos. Environ.*, *32*, 1111–1127.

Mihalas, D. (1978), *Stellar Atmospheres*, 2nd ed., 650 pp., W. H. Freeman, San Francisco, Calif.

Müller-Wodarg, I. C. F., R. V. Yelle, M. Mendillo, L. A. Young, and A. D. Aylward (2000), The thermosphere of Titan simulated by a global three-dimensional time-dependent model, *J. Geophys. Res.*, *105*, 20,833–20,856.

Müller-Wodarg, I. C. F., R. V. Yelle, N. Borggren, and J. H. Waite (2006), Waves and horizontal structures in Titan's thermosphere, *J. Geophys. Res.*, *111*, A12315, doi:10.1029/2006JA011961.

Müller-Wodarg, I. C. F., R. V. Yelle, J. Cui, and J. H. Waite (2008), Horizontal structures and dynamics of Titan's thermosphere, *J. Geophys. Res.*, *113*, E10005, doi:10.1029/2007JE003033.

Niemann, H. B., et al. (2005), The abundances of constituents of Titan's atmosphere from the GCMS instrument on the Huygens probe, *Nature*, *438*, 779–784.

Peraiah, A. (2001), *An Introduction to Radiative Transfer*, 492 pp., Cambridge Univ. Press, Cambridge, U. K.

Press, W. H., S. A. Teukolsky, W. T. Vetterling, and B. P. Flannery (1992), *Numerical Recipes in FORTRAN: The Art of Scientific Computing*, 2nd ed., Cambridge Univ. Press, Cambridge, U. K.

Press, W. H., S. A. Teukolsky, W. T. Vetterling, and B. P. Flannery (1996), *Numerical Recipes in FORTRAN 90: The Art of Parallel Computing*, 2nd ed., Cambridge Univ. Press, Cambridge, U. K.

Ralston, A., and P. Rabinowitz (1978), *A First Course in Numerical Analysis*, 2nd ed., Dover, New York.

Reid, R. C., J. M. Prausnitz, and B. E. Poling (1987), *Properties of Gases and Liquids*, 3rd ed., McGraw-Hill, New York.

Ridley, A. J., Y. Deng, and G. Tóth (2006), The global ionosphere thermosphere model, *J. Atmos. Terr. Phys.*, *68*, 839–864.

Robertson, I. P., et al. (2009), Structure of Titan's ionosphere: Model comparisons with Cassini data, *Planet. Space Sci.*, *57*, 1834–1846.

Roble, R. G., and E. C. Ridley (1994), A thermosphere-ionosphere-mesosphere-electrodynamics general circulation model (time-GCM): Equinox solar cycle minimum simulations (30–500 km), *Geophys. Res. Lett.*, *21*, 417–420.

Roble, R. G., E. C. Ridley, A. D. Richmond, and R. E. Dickinson (1988), A coupled thermosphere/ionosphere general circulation model, *Geophys. Res. Lett.*, *15*, 1325–1328.

Rogers, C., and P. G. Martin (1984), Half-range moment methods for radiative transfer in spherical geometry. III - Numerical solution and applications, *Astrophys. J.*, *284*, 327–336.

Rogers, C., and P. G. Martin (1986), Half-range moment methods for radiative transfer in spherical geometry. IV - Multifrequency problems with radiative equilibrium, *Astrophys. J.*, *311*, 800–804.

Rothman, L. S., et al. (1998), The HITRAN Molecular Spectroscopic Database and HAWKS (HITRAN Atmospheric Workstation): 1996 edition, *J. Quant. Spectrosc. Radiat. Transfer*, *60*, 665–710.

Rothman, L. S., et al. (2003), The HITRAN Molecular Spectroscopic Database: Edition of 2000 including updates through 2001, *J. Quant. Spectrosc. Radiat. Transfer*, *82*, 5–44.

Sagan, C., and W. R. Thompson (1984), Production and condensation of organic gases in the atmosphere of Titan, *Icarus*, *59*, 133–161.

Schunk, R., and A. F. Nagy (2000), *Ionospheres*, Cambridge Univ. Press, Cambridge, U. K.

Schunk, R. W. (1975), Transport equations for aeronomy, *Planet. Space Sci.*, *23*, 437–485.

Serway, R. A. (1996), *Physics for Scientists and Engineers*, Saunders Coll., Philadelphia, Penn.

Shah, M. B., C. J. Latimer, E. C. Montenegro, O. J. Tucker, R. E. Johnson, and H. T. Smith (2009), The implantation and interactions of O^+ in Titan's atmosphere: Laboratory measurements of collision-induced dissociation of N_2 and modeling of positive ion formation, *Astrophys. J.*, *703*, 1947–1954.

Shemansky, D. E., A. I. F. Stewart, R. A. West, L. W. Esposito, J. T. Hallett, and X. Liu (2005), The Cassini UVIS stellar probe of the Titan atmosphere, *Science*, *308*, 978–982.

Shippony, Z., and W. G. Read (1993), A highly accurate Voigt function algorithm, *J. Quant. Spectrosc. Radiat. Transfer*, *50*, 635–646.

Sillanpää, I., E. Kallio, R. Jarvinen, and P. Janhunen (2007), Oxygen ions at Titan's exobase in a Voyager 1-type interaction from a hybrid simulation, *J. Geophys. Res.*, *112*, A12205, doi:10.1029/2007JA012348.

Smith, F. I., and C. Smith (1972), Numerical evaluation of Chapman's grazing incidence integral ch(x, χ), *J. Geophys. Res.*, *77*, 3592–3597.

Smith, H. T., D. G. Mitchell, R. E. Johnson, and C. P. Paranicas (2009), Investigation of energetic proton penetration in Titan's atmosphere using the Cassini INCA instrument, *Planet. Space Sci.*, *57*, 1538–1546.

Sparks, L. (1997), Efficient line-by-line calculation of absorption coefficients to high numerical accuracy, *J. Quant. Spectrosc. Radiat. Transfer*, *57*, 631–650.

Strobel, D. F. (2006), Gravitational tidal waves in Titan's upper atmosphere, *Icarus*, *182*, 251–258.

Strobel, D. F. (2008), Titan's hydrodynamically escaping atmosphere, *Icarus*, *193*, 588–594.

Strobel, D. F. (2009), Titan's hydrodynamically escaping atmosphere: Escape rates and the structure of the exobase region, *Icarus*, *202*, 632–641.

Teanby, N. A., et al. (2007), Vertical profiles of HCN, HC$_3$N, and C$_2$H$_2$ in Titan's atmosphere derived from Cassini/CIRS data, *Icarus*, *186*, 364–384.

Teanby, N. A., et al. (2008), Global and temporal variations in hydrocarbons and nitriles in Titan's stratosphere for northern winter observed by Cassini/CIRS, *Icarus*, *193*, 595–611.

Thompson, W. J. (1993), Numerous neat algorithms for the Voigt profile function, *Comput. Phys.*, *7*, 627–631.

Tobiska, W. K. (1991), Revised solar extreme ultraviolet flux model, *J. Atmos. Terr. Phys.*, *53*, 1005–1018.

Tobiska, W. K., and C. A. Barth (1990), A solar EUV flux model, *J. Geophys. Res.*, *95*, 8243–8251.

Torr, D. G., M. R. Torr, H. C. Brinton, L. H. Brace, N. W. Spencer, A. E. Hedin, W. B. Hanson, J. H. Hoffman, A. O. Nier, and J. C. G. Walker (1979), An experimental and theoretical study of the mean diurnal variation of O$^+$, NO$^+$, O2$^+$, and N2$^+$ ions in the mid-latitude F1 layer of the ionosphere, *J. Geophys. Res.*, *84*, 3360–3372.

Tucker, O. J., and R. E. Johnson (2009), Thermally driven atmospheric escape: Monte Carlo 3 simulations for Titan's atmosphere, *Planet. Space Sci.*, *57*, 1889–1894.

Vinatier, S., et al. (2007), Vertical abundance profiles of hydrocarbons in Titan's atmosphere at 15°S and 80°N retrieved from Cassini/CIRS spectra, *Icarus*, *188*, 120–138.

Vuitton, V., R. V. Yelle, and V. G. Anicich (2006), The nitrogen chemistry of Titan's upper atmosphere revealed, *Astrophys. J.*, *647*, L175–L178.

Vuitton, V., R. V. Yelle, and J. Cui (2008), Formation and distribution of benzene on Titan, *J. Geophys. Res.*, *113*, E05007, doi:10.1029/2007JE002997.

Wahlund, J.-E., et al. (2005), Cassini measurements of cold plasma in the ionosphere of Titan, *Science*, *308*, 986–989.

Waite, J. H., et al. (2005), Ion Neutral Mass Spectrometer results from the first flyby of Titan, *Science*, *308*, 982–986.

Waite, J. H., et al. (2006), Cassini Ion and Neutral Mass Spectrometer: Enceladus plume composition and structure, *Science*, *311*, 1419–1422.

Waite, J. H., D. T. Young, T. E. Cravens, A. J. Coates, F. J. Crary, B. Magee, and J. Westlake (2007), The process of tholin formation in Titan's upper atmosphere, *Science*, *316*, 870–875.

Waite, J. H., Jr., et al. (2009), Liquid water on Enceladus from observations of ammonia and ^{40}Ar in the plume, *Nature*, *460*, 487–490.

Weast, R. C. (1984), *CRC Handbook of Chemistry and Physics*, CRC Press, Boca Raton, Fla.

Wilson, E. H. (2002), Investigations into the photochemistry of the current and primordial atmosphere of Titan, Ph.D. thesis, Univ. of Mich., Ann Arbor.

Wilson, E. H., and S. K. Atreya (2004), Current state of modeling the photochemistry of Titan's mutually dependent atmosphere and ionosphere, *J. Geophys. Res.*, *109*, E06002, doi:10.1029/2003JE002181.

Yaws, C. L. (1995), *Handbook of Transport Property Data, Viscosity, Thermal Conductivity, and Diffusion Coefficients of Liquids and Gases*, Butterworth-Heinemann, Burlington, Mass.

Yaws, C. L. (1997), *Handbook of Thermal Conductivity*, vol. 4, *Inorganic Compounds and Elements*, Gulf, Houston, Tex.

Yelle, R. V. (1991), Non-LTE models of Titan's upper atmosphere, *Astrophys. J.*, *383*, 380–400.

Yelle, R. V., N. Borggren, V. de La Haye, W. T. Kasprzak, H. B. Niemann, I. Müller-Wodarg, and J. H. Waite (2006), The vertical structure of Titan's upper atmosphere from Cassini Ion Neutral Mass Spectrometer measurements, *Icarus*, *182*, 567–576.

Yelle, R. V., J. Cui, and I. C. F. Müller-Wodarg (2008), Methane escape from Titan's atmosphere, *J. Geophys. Res.*, *113*, E10003, doi:10.1029/2007JE003031.

A. Bar–Nun, Department of Geophysics and Planetary Sciences, Tel Aviv University, Tel Aviv 69978, Israel.

A. D. DeJong and J. Westlake, Department of Physics and Astronomy, University of Texas at San Antonio, San Antonio, TX 78249, USA.

J. M. Bell, V. De La Haye, B. A. Magee, K. E. Mandt, and J. H. Waite Jr., Division of Space Science and Engineering, Southwest Research Institute, 6220 Culebra Rd., PO Box 28510, San Antonio, TX 78228, USA.

S. W. Bougher, A. J. Ridley, and G. Toth, Department of Atmospheric, Oceanic, and Space Sciences, University of Michigan, Ann Arbor, MI 48109, USA.

R. Jacovi, Ice Spectroscopy Laboratory, Jet Propulsion Laboratory, California Institute of Technology, 4800 Oak Grove Dr., Pasadena, CA 91109, USA.